

Fermilab-Pub-98/077-T
 McGill/98-6
 hep-ph/9803410

Deconstructing Angular Correlations in ZH , ZZ , and WW Production at LEP2

Gregory Mahlon*

*Department of Physics, McGill University,
 3600 University St., Montréal, QC H3A 2T8
 Canada*

Stephen Parke†

*Department of Theoretical Physics
 Fermi National Accelerator Laboratory
 P.O. Box 500, Batavia, IL 60510
 USA*

(March 20, 1998)

Abstract

We apply a generalized spin-basis analysis to associated Higgs production and gauge boson pair production at LEP. This framework allows us to identify a choice of spin axes for the processes $e^+e^- \rightarrow ZH, ZZ$ which leads to strikingly different correlations among the decay products, even well above threshold. This spin basis optimizes the difference in the angular correlations for these two processes. In contrast, the same distributions display little contrast when the helicity basis is used. We also apply this technique to the case of W boson pair production.

I. INTRODUCTION

The search for a light Higgs boson and the study of gauge boson pair production [1] are important physics goals of the LEP2 upgrade at CERN. If kinematically accessible to LEP2, the Higgs boson will be primarily produced via the Bjorken process $e^+e^- \rightarrow ZH$ [2,3]. An irreducible physics background to this processes is the production of Z boson pairs, which is most troublesome when $M_H \sim M_Z$. The clear separation of these two processes is required for a convincing Higgs boson discovery or lower bound mass limit. Kinematics as well as characteristic angular correlations will be useful in this separation. The study of W boson pair production is also interesting in its own right [4–6], as it involves vertices coupling three gauge bosons (especially ZW^+W^-), vertices which to date are poorly-probed experimentally. These couplings may be probed with varying degrees of sophistication by testing the predictions for the total cross section, production angle distribution, and correlations among the vector boson decay products. Hence for all of these processes, $e^+e^- \rightarrow ZH, ZZ$ and WW , we are keenly interested in the angular correlations among the final state particles. To disentangle these correlations it is very useful to understand the spin correlations of the heavy particles produced. These spin correlations as well as the subsequent correlations of the decay products are the focus of this paper.

Until recently, most spin-related studies were carried out within the framework provided by the zero momentum frame helicity basis (see, for example Refs. [3–6]). For particles which are ultra-relativistic, this is appropriate. However, for particles which are only moderately relativistic, there is no reason to expect that the helicity basis will produce the best description of the physics involved. Indeed, for the case of $t\bar{t}$ production at low energy $p\bar{p}$ and e^+e^- colliders, it was shown in Refs. [7–9] that the helicity basis is far from optimal. In this paper we use the generalized spin basis introduced in Ref. [8] to describe ZH, ZZ , and WW production and decay at LEP2 energies. In particular, we write the polarized production amplitudes in terms of the most general CP -conserving choice of spin axes, and from these expressions determine the choice of axes which leads to the most distinctive correlations among the final state particles. We argue that it is advantageous at LEP2 energies to tune the choice of spin axis to the experimental issue being investigated, rather than to simply use the helicity basis and try to unravel the contributions from what are in many cases nearly-equally populated spin states.

Much effort in the literature has been devoted to the analysis of various anomalous trilinear couplings [5,6,10], employing, of course, the helicity basis. Rather than attempt to rework all of those studies in terms of the generalized spin-basis, we have chosen to concentrate on the picture within the Standard Model. It is clear from our results, however, that such a study would be worthwhile, as we expect different spin bases to be optimal for the extraction/limitation of different anomalous couplings. Such an analysis would be a major extension of this work.

The remainder of this paper is organized as follows. After a brief discussion of our notation and conventions in Sec. II, we consider the ZH/ZZ system within the generalized spin basis framework (Sec. III). For each process, we consider in detail the polarized production cross sections, and construct spin bases suggested by the expressions for the amplitudes. We consider the decay of polarized Z 's, and then link the production and decay to study the correlations among the decay products. We are able to construct a basis in which these

correlations differ significantly for the ZH and ZZ cases, whereas in the helicity basis the correlations are virtually non-existent. Sec. IV contains the corresponding analysis for the W^+W^- system. In this case, matters are less clear-cut, and we present several suggestions for bases which may be useful under different circumstances. Finally, Sec. V contains our conclusions. Explicit expressions for the polarization vectors we employ for the massive vector bosons in the generalized spin basis appear in the Appendix.

II. NOTATION AND CONVENTIONS

To describe the polarized production cross sections for ZH , ZZ , and WW discussed in this paper, we employ the generic spin basis introduced by Parke and Shadmi in Ref. [8], as illustrated in Fig. 1. For ZZ and WW , this is the most general basis which conserves CP . We label the two particles produced in the collision by P_1 and P_2 . The zero momentum frame (ZMF) production angle θ^* is defined as the angle between the electron and P_1 directions. The spin states for the first particle are defined in its rest frame, where we decompose the P_1 spin along the direction \hat{s}_1 , which makes an angle ξ with the P_2 momentum in the clockwise direction. Likewise, the P_2 spin states are defined in its rest frame along the direction \hat{s}_2 , which makes the *same* angle ξ with the P_1 momentum, also in the clockwise direction. We denote the two transverse polarization states by $+$ and $-$ and the longitudinal state by 0. Throughout this paper we use the terms “transverse” and “longitudinal” to refer to directions relative to the spin axis, *not* the direction of motion of the particle. A generic vector boson spin will be designated by λ . If we sum over all of the polarizations of the vector boson(s), then the dependence on ξ drops out of the result.

Note that although the Higgs boson is a scalar, we may still define a spin axis for it as if it were a vector. The spin zero character of the Higgs will be reflected in a lack of any dependence on the choice of this axis.

Within the generic spin basis framework, specific spin bases are defined by stating the relationship between ξ and θ^* (and any other relevant event parameters). For example, the ubiquitous helicity basis is defined by fixing

$$\xi \equiv \pi. \quad (1)$$

In this case, the spins are defined along the directions of motion of the particles as seen in the ZMF.

Another interesting basis is the beamline basis [7], which is defined by

$$\sin \xi = \frac{\sqrt{1-\beta^2} \sin \theta^*}{1 - \beta \cos \theta^*}; \quad \cos \xi = \frac{\cos \theta^* - \beta}{1 - \beta \cos \theta^*}. \quad (2)$$

Here β is the ZMF speed of P_1 . In this basis, the spin axis for P_1 is the electron direction. Furthermore, if P_1 and P_2 have identical mass, then the spin axis for P_2 is the positron direction.

Later in this paper, we will encounter additional bases, whose definitions are inspired by the form of the matrix elements for the processes under consideration.

Except for the fermion masses, which we set equal to zero, all input masses and coupling constants used in the computations presented in this paper are the central values as reported

in the 1996 Review of Particle Properties [11]. Furthermore, we also neglect the coupling between the electron and Higgs.

III. THE PROCESSES $e^+e^- \rightarrow ZH, ZZ$ AT LEP

If the Higgs is light enough to be observed at LEP2, then its production will be dominated by the process $e^+e^- \rightarrow ZH$, for which the largest background is $e^+e^- \rightarrow ZZ$. This suggests the potential for difficulties should the Higgs mass lie too close to the mass of the Z . In particular, at $\sqrt{s} = 192$ GeV, the tree-level cross section for ZH is only 0.5 pb when $M_H = M_Z$, compared to 1.2 pb for ZZ . As noted by Brown [12], this situation improves if b -tagging is employed, as the Higgs decays mainly to $b\bar{b}$ whereas the Z decays to this final state only 15% of the time. Rather than rely on b -tagging, Kunszt and Stirling [13] have considered the distribution of the angle that the decay leptons in $e^+e^- \rightarrow ZH/ZZ \rightarrow \ell\bar{\ell}$ jets. make with the direction of the beam in the ZMF. They find a significant difference in this distribution in the ZH and ZZ cases. Finally, Summers [14] has added the effect of polarizing the beams on the distribution of Ref. [13].

In this section we examine the ZH and ZZ processes within the generalized spin basis framework. We begin in Sec. III A by analyzing the polarized production amplitudes for the process $e^+e^- \rightarrow ZH$ in great detail. The expressions for these amplitudes will show us how to construct a basis in which only transversely-polarized Z 's are produced in association with the Higgs. In Sec. III B we present polarized production amplitudes for $e^+e^- \rightarrow ZZ$. After describing the decay of polarized Z 's (Sec. III C), we combine the production and decay information to discuss the angular correlations among the decay products in the ZH/ZZ system (Sec. III D). Our analysis shows that the angular variable suggested by Kleiss and Stirling [13], while close to optimal, may be improved upon, especially as the ZH pair is produced further and further above threshold. In particular, we find that in the basis constructed in Sec. III A, certain decay angular distributions are very different for ZH versus ZZ . In contrast, these same distributions are nearly featureless in the helicity basis. We conclude this part of the paper in Sect. III E with a brief look at how the production of a pseudoscalar Higgs would differ from the Standard Model Higgs.

Although we focus on the case where $M_H \sim M_Z$, our results are more general, since the existence of our optimized basis for $e^+e^- \rightarrow ZH$ depends only on that process being kinematically allowed. It is also potentially useful at the Tevatron, because the amplitude for $q\bar{q}' \rightarrow WH$ has the same spin structure as the amplitude for $e^+e^- \rightarrow ZH$.

A. Polarized ZH Production

To describe the process $e^+e^- \rightarrow ZH$, we take particle P_1 in Fig. 1 to be the Z , and particle P_2 to be the Higgs. In general, the Higgs and Z have different masses (M_H and M_Z respectively), leading to the following connection between the center-of-mass energy \sqrt{s} and speed β_Z of the Z boson:

$$\beta_Z = \frac{\sqrt{[s - (M_Z + M_H)^2][s - (M_Z - M_H)^2]}}{s - M_H^2 + M_Z^2}. \quad (3)$$

Rather than use Eq. (3) to eliminate one of s or β_Z from our expressions, it is more convenient to use both quantities.

If we neglect the electron mass, there is but a single diagram for $e^+e^- \rightarrow ZH$. It leads to the differential cross section¹

$$\frac{d\sigma^\lambda(e^+e^- \rightarrow ZH)}{d(\cos \theta^*)} = \frac{G_F^2 M_W^2}{\cos^2 \theta_W} \frac{\beta_Z \gamma_Z M_Z^3}{32\pi s^{3/2}} \left(\frac{s + M_Z^2 - M_H^2}{s - M_Z^2} \right)^2 \times \left\{ \cos^2 2\theta_W [\mathcal{S}_L^\lambda(\beta_Z, \theta^*, \xi)]^2 + 4 \sin^4 \theta_W [\mathcal{S}_R^\lambda(\beta_Z, \theta^*, \xi)]^2 \right\} \quad (4)$$

where G_F is the Fermi coupling constant, M_W is the mass of the W boson, θ_W is the Weinberg angle, and γ_Z is the usual relativistic factor, $\gamma_Z = (1 - \beta_Z^2)^{-1/2}$. The two terms in the curly brackets come from the two possible chiralities of the initial electron line. All of the spin information is contained in the spin functions, $\mathcal{S}_{L,R}^\lambda$, which are given by

$$\mathcal{S}_L^\pm(\beta_Z, \theta^*, \xi) = \mathcal{S}_R^\mp(\beta_Z, \theta^*, \xi) = \frac{1}{\sqrt{2}} \left[\sin \theta^* \sin \xi + \sqrt{1 - \beta_Z^2} (\cos \theta^* \cos \xi \pm 1) \right] \quad (5)$$

and

$$\mathcal{S}_L^0(\beta_Z, \theta^*, \xi) = \mathcal{S}_R^0(\beta_Z, \theta^*, \xi) = \sqrt{1 - \beta_Z^2} \cos \theta^* \sin \xi - \sin \theta^* \cos \xi. \quad (6)$$

Summing over the three possible spins of the Z we obtain the total (unpolarized) differential cross section

$$\sum_\lambda \frac{d\sigma^\lambda}{d(\cos \theta^*)} = \frac{G_F^2 M_W^2}{\cos^2 \theta_W} \frac{\beta_Z \gamma_Z M_Z^3}{32\pi s^{3/2}} \left(\frac{s + M_Z^2 - M_H^2}{s - M_Z^2} \right)^2 \times \left\{ 1 - 4 \sin^2 \theta_W + 8 \sin^4 \theta_W \right\} \left\{ 2(1 - \beta_Z^2) + \beta_Z^2 \sin^2 \theta^* \right\}. \quad (7)$$

Eq. (7) is independent of the spin axis angle ξ , as it must be.

Since, in general, at each value of θ^* we are allowed to choose a different value of ξ , it is useful to plot these amplitudes in the $\cos \theta^*$ - $\cos \xi$ plane. Consequently, we define the quantity

$$f^\lambda(\beta_Z, \theta^*, \xi) \equiv \frac{\frac{d\sigma^\lambda(\beta_Z, \theta^*, \xi)}{d(\cos \theta^*)}}{\sum_{\lambda'} \frac{d\sigma^{\lambda'}(\beta_Z, \theta^*, \xi)}{d(\cos \theta^*)}}, \quad (8)$$

which is the fraction of the total cross section coming from the spin state λ . In Fig. 2 we have plotted $f^\lambda(\beta_Z, \theta^*, \xi)$ for a collider energy $\sqrt{s} = 192$ GeV and Higgs mass $M_H = M_Z$. These plots illustrate the features of the amplitude discussed below, and are an indispensable aid when the amplitude becomes complicated, as in the ZZ and WW cases.

¹All cross sections given in this paper are spin-averaged for the incoming particles.

For $\xi = \pi$, we recover the usual helicity basis expressions from Eqs. (4)–(6):

$$\begin{aligned}\mathcal{S}_L^\pm(\beta_Z, \theta^*, \pi) &= \mathcal{S}_R^\mp(\beta_Z, \theta^*, \pi) = \frac{1}{\sqrt{2}}\sqrt{1-\beta_Z^2}(\pm 1 - \cos \theta^*); \\ \mathcal{S}_L^0(\beta_Z, \theta^*, \pi) &= \mathcal{S}_R^0(\beta_Z, \theta^*, \pi) = \sin \theta^*. \end{aligned}\quad (9)$$

At high energy, the transverse amplitudes die off, leaving only the longitudinal amplitude.

An examination of Eq. (5) reveals that it is not possible to make both of the transverse spin functions \mathcal{S}_L^λ and \mathcal{S}_R^λ vanish simultaneously. Consequently, it is impossible to make either of the transverse amplitudes of Eq. (4) vanish. There is, however, a zero in the longitudinal contribution, Eq. (6), which results from choosing

$$\sin \xi = \frac{\sin \theta^*}{\sqrt{1 - \beta_Z^2 \cos^2 \theta^*}}; \quad \cos \xi = \frac{\sqrt{1 - \beta_Z^2} \cos \theta^*}{\sqrt{1 - \beta_Z^2 \cos^2 \theta^*}}, \quad (10)$$

i.e. $\tan \xi = \gamma_Z \tan \theta^*$. The basis corresponding to this choice, the ZH -transverse basis, will turn out to be very useful in the study of ZH events. The nonvanishing spin functions in the ZH -transverse basis are

$$\begin{aligned}\mathcal{S}_L^\pm(\beta_Z, \theta^*, \tan^{-1}(\gamma_Z \tan \theta^*)) &= \mathcal{S}_R^\mp(\beta_Z, \theta^*, \tan^{-1}(\gamma_Z \tan \theta^*)) \\ &= \frac{1}{\sqrt{2}} \left[\sqrt{1 - \beta_Z^2 \cos^2 \theta^*} \pm \sqrt{1 - \beta_Z^2} \right]. \end{aligned}\quad (11)$$

These functions are completely flat in $\cos \theta^*$ at threshold, and become proportional to $\sin \theta^*$ for $\beta_Z \rightarrow 1$. Note that the existence of this basis does not depend on either the machine energy or the Higgs mass: Eqs. (3) and (10) remain well-defined so long as $\sqrt{s} \geq M_Z + M_H$. In particular, for $\beta_Z \rightarrow 1$, we have

$$\sin \xi \rightarrow 1; \quad \cos \xi \rightarrow 0, \quad (12)$$

that is, $\xi \rightarrow \pi/2$. This is clearly *not* the helicity basis.² The ZH -transverse basis is also the basis in which the + and – components are each maximized.

For completeness, we mention the ZH -longitudinal basis, defined by $\tan \xi = -\gamma_Z^{-1} \cot \theta^*$. As its name suggests, the ZH -longitudinal basis maximizes the fraction of longitudinal Z 's. This basis is potentially useful for large values of β_Z since the fraction of longitudinal Z 's with increasing energy approaches unity faster than in the helicity basis.

In Table I, we list the contributions to the total amplitude for each of the three possible Z spins as measured in the helicity, beamline, ZH -transverse, and ZH -longitudinal bases. We employ a center-of-mass energy $\sqrt{s} = 192$ GeV and a Higgs mass $M_H = M_Z$, the value which makes separation of ZH and ZZ events the most difficult. Note that in the helicity

²The absence of any longitudinal contribution whatsoever, even at high energy, does not represent a violation of the vector boson equivalence theorem, which is really a statement about the helicity basis.

basis, the three spin states are populated nearly equally. As we shall see below, this feature makes the helicity basis a very poor choice for studying the ZH/ZZ system.

Because the Higgs mass is still unknown, we might worry that the predictions for the spin compositions would depend strongly on M_H , rendering this discussion pointless. For any particular machine energy and Higgs mass, Eq. (3) tells us the appropriate value of β_Z to use. In Fig. 3 we have plotted the fractional contribution of each of the three spin components as a function of β_Z for the helicity, beamline, ZH -transverse, and ZH -longitudinal bases. We see that in the ZH -transverse basis, the spin composition is remarkably flat as a function of β_Z , except near $\beta_Z = 1$. In fact, for $M_H \gtrsim 70$ GeV, $\beta_Z \lesssim 0.5$ when $\sqrt{s} = 192$ GeV. So, for the values of M_H and \sqrt{s} accessible at LEP, the spin composition in the ZH -transverse basis is effectively constant. Contrast this to the beamline basis, which actually coincides with the ZH -transverse basis at $\beta_Z = 0$ and the helicity basis for $\beta_Z \rightarrow 1$! In this case, the spin composition is not particularly stable.

A second reason for preferring a basis in which the spin composition is stable with respect to changes in β_Z relates to the effects of initial state radiation (ISR). Although we have neglected these effects in our computations, it is apparent what should happen qualitatively: some of the observed events will be produced from e^+e^- pairs with a center-of-mass energy lower than the machine energy. Therefore, the smaller the dependence on β_Z , the less sensitive the breakdowns will be to the effects of ISR.

Finally, in Fig. 4 we compare the production angular distributions of the polarized cross sections in the helicity and ZH -transverse bases. We see that in the helicity basis, the identity of the dominant component depends on $\cos \theta^*$, whereas in the ZH -transverse basis, the ratio of the two non-vanishing amplitudes is essentially constant.

B. Polarized ZZ Production

We now turn to the process $e^+e^- \rightarrow ZZ$. With our comparison to ZH production in mind, we identify the Z which decays leptonically with P_1 and the Z which decays to $b\bar{b}$ with P_2 in Fig. 1.

The only diagrams for ZZ production are t -channel electron exchange diagrams, one for each ordering of the two Z 's. For an initial fermion pair with left-handed chirality we have

$$\frac{d\sigma_L^{\lambda\bar{\lambda}}(e^+e^- \rightarrow ZZ)}{d(\cos \theta^*)} = \frac{G_F^2 M_W^4}{32\pi M_Z^2} \frac{\cos^4 2\theta_W}{16 \cos^4 \theta_W} \beta \gamma^2 \left[\frac{\mathcal{S}_L^{\lambda\bar{\lambda}}(\beta, \theta^*, \xi)}{1-2\beta \cos \theta^* + \beta^2} + \frac{\mathcal{S}_L^{\lambda\bar{\lambda}}(-\beta, \theta^*, \xi)}{1+2\beta \cos \theta^* + \beta^2} \right]^2, \quad (13)$$

while the result for right-handed chirality reads

$$\frac{d\sigma_R^{\lambda\bar{\lambda}}(e^+e^- \rightarrow ZZ)}{d(\cos \theta^*)} = \frac{G_F^2 M_W^4}{32\pi M_Z^2} \frac{\sin^8 \theta_W}{\cos^4 \theta_W} \beta \gamma^2 \left[\frac{\mathcal{S}_R^{\lambda\bar{\lambda}}(\beta, \theta^*, \xi)}{1-2\beta \cos \theta^* + \beta^2} + \frac{\mathcal{S}_R^{\lambda\bar{\lambda}}(-\beta, \theta^*, \xi)}{1+2\beta \cos \theta^* + \beta^2} \right]^2. \quad (14)$$

These expressions contain the common ZMF speed of the two Z 's, which is connected to the center-of-mass energy by

$$\beta = \sqrt{1 - 4M_Z^2/s}. \quad (15)$$

We have not combined the pairs of terms appearing in the square brackets in order to make manifest the similarities to the W -pair amplitudes presented in Sec. IV.

All of the spin information is contained in the spin functions, $\mathcal{S}_{L,R}^{\lambda\bar{\lambda}}$, which may be written as

$$\mathcal{S}_L^{+-}(\beta, \theta^*, \xi) = 2\mathcal{G}_1(\beta, \theta^*, \xi)\mathcal{G}_2(\beta, \theta^*, \xi) \quad (16)$$

$$\mathcal{S}_L^{++}(\beta, \theta^*, \xi) = 2\mathcal{G}_3(\beta, \theta^*, \xi)\mathcal{G}_4(\beta, \theta^*, \xi) \quad (17)$$

$$\mathcal{S}_L^{+0}(\beta, \theta^*, \xi) = \mathcal{S}_L^{0-}(\beta, \theta^*, \xi) = \sqrt{2}[\mathcal{G}_1(\beta, \theta^*, \xi)\mathcal{G}_4(\beta, \theta^*, \xi) - \mathcal{G}_2(\beta, \theta^*, \xi)\mathcal{G}_3(\beta, \theta^*, \xi)] \quad (18)$$

$$\mathcal{S}_L^{00}(\beta, \theta^*, \xi) = 2\beta \sin \theta^* (1 - 2\beta \cos \theta^* + \beta^2) - 4\mathcal{G}_3(\beta, \theta^*, \xi)\mathcal{G}_4(\beta, \theta^*, \xi) \quad (19)$$

where

$$\begin{aligned} \mathcal{G}_1(\beta, \theta^*, \xi) &= (1 + \cos \theta^* \cos \xi + \sqrt{1-\beta^2} \sin \theta^* \sin \xi) - \beta(\cos \theta^* + \cos \xi) \\ \mathcal{G}_2(\beta, \theta^*, \xi) &= (\sin \theta^* \cos \xi - \sqrt{1-\beta^2} \cos \theta^* \sin \xi) + \beta(\sin \theta^* + \sqrt{1-\beta^2} \sin \xi) \\ \mathcal{G}_3(\beta, \theta^*, \xi) &= \sin \xi(\beta - \cos \theta^*) + \sqrt{1-\beta^2} \sin \theta^* \cos \xi \\ \mathcal{G}_4(\beta, \theta^*, \xi) &= \sin \theta^* \sin \xi - \sqrt{1-\beta^2} \cos \xi(\beta - \cos \theta^*). \end{aligned} \quad (20)$$

Since the replacement $\xi \rightarrow \xi + \pi$ has the effect of interchanging the $+$ and $-$ states, expressions for the remaining spin combinations may be obtained from the relation

$$\mathcal{S}_L^{\lambda\bar{\lambda}}(\beta, \theta^*, \xi) = \mathcal{S}_L^{-\lambda, -\bar{\lambda}}(\beta, \theta^*, \xi + \pi). \quad (21)$$

The total differential cross section is remarkably simple. Summing over the spins of both Z 's and including both fermion chiralities we obtain

$$\begin{aligned} \sum_{\lambda, \bar{\lambda}, C} \frac{d\sigma_C^{\lambda\bar{\lambda}}}{d(\cos \theta^*)} &= \frac{G_F^2 M_W^4}{16\pi M_Z^2 \cos^4 \theta_W} (\cos^4 2\theta_W + 16 \sin^8 \theta_W) \\ &\times \beta(1 - \beta^2) \frac{2(1 - \beta^2)^3 + \beta^2[8 + (1 - \beta^2)^2] - 4\beta^4 \sin^4 \theta^*}{[(1 - \beta^2)^2 + 4\beta^2 \sin^2 \theta^*]^2}. \end{aligned} \quad (22)$$

Of the nine spin configurations, there are only six which are independent, since CP invariance forces the equality of the $(++)$ and $(--)$ components, as well as the equality of the (± 0) and $(0\mp)$ components [5]. Therefore, for the rest of the paper we will refer to $[(++) + (--)]$, $[(+0) + (0-)]$, and $[(0+)] + (0-)]$ as single components.

One of the ways which the C and P violation present in the weak interactions manifests itself as the different prefactors in Eqs. (13) and (14). The spin functions, on the other hand, obey these symmetries, and are connected by

$$\mathcal{S}_R^{\lambda\bar{\lambda}}(\beta, \theta^*, \xi) = \mathcal{S}_L^{-\lambda, -\bar{\lambda}}(\beta, \theta^*, \xi). \quad (23)$$

Because of the somewhat complicated form of the amplitudes, it is instructive to plot the amplitudes for each of the six independent spin configurations in the $\cos\theta^*$ - $\cos\xi$ plane. In Fig. 5, we have plotted the quantity³

$$f^{\lambda\bar{\lambda}}(\beta, \theta^*, \xi) \equiv \frac{\frac{d\sigma^{\lambda\bar{\lambda}}(\beta, \theta^*, \xi)}{d(\cos\theta^*)}}{\sum_{\lambda'\bar{\lambda}'} \frac{d\sigma^{\lambda'\bar{\lambda}'}(\beta, \theta^*, \xi)}{d(\cos\theta^*)}} \quad (24)$$

(*i.e.* the fraction of the total amplitude in a given spin configuration) for a machine center-of-mass energy of 192 GeV. Visible in the plots is the fact that the (00) contribution is exactly twice the [(++) + (--)] contribution for all values of θ^* and ξ [see Eqs. (13), (17) and (19)]. Also noteworthy are the broad minima in the (+-), (-+), (00), and [(++) + (--)] components in the vicinity of the diagonal.⁴ The [(+0) + (0-)] and [(0+) + (0-)] contributions have corresponding maxima in this region.

In Table II we give the fraction of the total amplitude coming from each of the six independent spin configurations in the four bases tabulated for ZH . In two of the bases (helicity and ZH -longitudinal), the high degree of symmetry present in Eqs. (13) and (14) resulting from the two identical final state particles manifests as the equalities $(+-) = (-+)$ and $[(+0) + (0-)] = [(0+) + (-0)]$. It is important to note that we *define* the ZH -transverse basis in terms of Eqs. (3) and (10), even when we are dealing with ZZ production. Thus, the spin breakdowns in this basis depend on the Higgs mass via the value assigned to β_Z . For $\beta_Z \lesssim 0.5$ (the interesting region), the curve traced out by the ZH -transverse basis in the $\cos\theta^*$ - $\cos\xi$ plane lies near the diagonal, an area in the $\cos\theta^*$ - $\cos\xi$ plane where the contributions from the various spins are relatively stable. Thus, it is not surprising to find that for $\beta_Z \lesssim 0.5$ and $\sqrt{s} = 192$ GeV, there are no significant deviations from the entries for the ZH -transverse basis in Table II.

In Fig. 6 we have plotted the fraction of the total amplitude in each of the spin components using the helicity and ZH -transverse bases as a function of β . In the helicity basis, we find that the (+-) and (-+) contributions are always equal, as are the [(+0) + (0-)] and [(0+) + (-0)] contributions. Consequently, if we look at the population of the spin states for one of the Z 's while summing over the other Z , we find that the + and - states are populated equally. Furthermore, at threshold, this inclusive breakdown is precisely 1/3 for each spin, and this changes relatively slowly with increasing β . The situation is considerably better in the ZH -transverse basis, where no two of the six spin contributions are equal, and where there is a reasonable difference in the inclusive contributions. While we have used $\beta_Z = \beta$ (*i.e.* $M_H = M_Z$) in preparing these plots, we have verified that for the range accessible to LEP, the dependence on the Higgs mass is inconsequential.

³Implicit in this definition is a sum (in both numerator and denominator) over the chirality of the initial electron line.

⁴None of these components actually vanish in this region.

In Fig. 7 we compare the angular distributions of the polarized production cross sections in the helicity and ZH -transverse bases at $\sqrt{s} = 192$ GeV. In the helicity basis there is a complicated interplay among the six spin components, whereas in the ZH -transverse basis the two dominant components appear in approximately the same ratio, independent of $\cos\theta^*$.

C. Polarized Decays

The $Zf\bar{f}$ coupling violates both parity and flavor universality. Thus, the angular distributions for the decay of polarized Z bosons are forward-backward asymmetric, and depend on which fermions appear in the final state. Neglecting the mass of the final state fermions,⁵ we obtain the following angular distributions in the rest frame of the decaying Z :

$$\frac{1}{\Gamma_f} \frac{d\Gamma^\pm}{d(\cos\chi)} = \frac{3}{8} [\alpha_f(1 \mp \cos\chi)^2 + (1 - \alpha_f)(1 \pm \cos\chi)^2] \quad (25)$$

for the transverse polarizations and

$$\frac{1}{\Gamma_f} \frac{d\Gamma^0}{d(\cos\chi)} = \frac{3}{4} \sin^2\chi \quad (26)$$

for the longitudinal polarization. These distributions have been normalized to unit area by inclusion of the partial width Γ_f for the decay $Z \rightarrow f\bar{f}$. We take χ to be the angle between the direction of motion of the fermion and the spin axis as seen in the Z rest frame, and absorb the dependence on the couplings between left- and right-handed chirality fermions to the Z into the factor α_f . For convenience, we have collected the values of α_f in Table III. The corresponding distributions are plotted in Fig. 8. Unfortunately, the decays with the most distinct distributions, $Z \rightarrow \nu\bar{\nu}$ are invisible. Furthermore, charge and flavor identification for decays to quarks (which appear as two jets) is virtually impossible, except perhaps for b quarks. For $Z \rightarrow \ell\bar{\ell}$, we have a fairly large overlap between the $+$ and $-$ distributions. All of these features lead us to conclude that it may not be possible to distinguish between the $+$ and $-$ polarizations. However, as we shall see below, the difference between the \pm and 0 states is sufficient for separating ZH and ZZ , provided that the appropriate spin basis is used.

Naturally, since the Higgs is a scalar, its decay angle distributions will be completely flat.

D. Correlations

In this section we will put everything together to discuss the correlations among the ZH/ZZ decay products. For concreteness, we take the final state to be $\ell\bar{\ell}b\bar{b}$, the $\ell\bar{\ell}$ coming

⁵Inclusion of the finite mass effects would result in straightforward but messy modifications to Eqs. (25) and (26). These effects are greatest for b -quarks, where they are less than a few percent.

from a decaying Z , and the $b\bar{b}$ from the Higgs or other Z . The results we present do not change very much if we consider a $q\bar{q}b\bar{b}$ final state: since it is not possible to tell which light jet is the q and which is the \bar{q} , all distributions in the Z decay angle χ_Z defined below would be symmetric about $\cos \chi_Z = 0$. On the other hand, α_ℓ is only slightly larger than $1/2$, leading to small asymmetries between positive and negative values of $\cos \chi_Z$.

In order to display the advantages of using the ZH -transverse basis defined by Eq. (10), we consider a scatter plot in the decay angles χ_Z and χ_H , defined as follows. On the $Z \rightarrow \ell\bar{\ell}$ side of the event, let χ_Z be the angle between the ℓ emission direction and the Z spin axis in the Z rest frame. On the $Z/H \rightarrow b\bar{b}$ side of the event, let χ_H be the angle between the b emission direction⁶ and the Z/H spin axis in the Z/H rest frame. In Fig. 9 we present this distribution for ZH and ZZ production for the helicity and ZH -transverse bases for $\sqrt{s} = 192$ GeV and $M_H = M_Z$. The difference between the two plots is dramatic: in the helicity basis, the two distributions are nearly flat, while there is significant structure when the ZH -transverse basis is used. This difference is underscored by the plots in Fig. 10, which compare the 1-dimensional distributions in $\cos \chi_Z$ and $\cos \chi_H$. Clearly, the angular information contained in an analysis employing the ZH -transverse basis provides a useful handle in the separation of ZH and ZZ events, even when $M_H \sim M_Z$. In contrast, the helicity angles are virtually useless in this respect!

Kunszt and Stirling [13] have noted significant angular correlations in the ZMF between the direction of the final state muons and the beam direction. Effectively this is the beamline basis. At threshold, the beamline basis coincides with the optimal (ZH -transverse) basis, and the ZMF coincides with the Z rest frame. At LEP2, $\beta \sim 1/3$, *i.e.* not that far above threshold. Thus, even though they don't use the optimal basis, Kunszt and Stirling do see non-trivial angular correlations. The largest possible correlations, however, are obtained using the muon direction relative to the ZH -transverse basis spin axis in the Z rest frame. Furthermore, the gap between their distribution and the optimal one widens as we move further above threshold.

The amplitudes for the processes $e^+e^- \rightarrow ZH/ZZ \rightarrow \mu^+\mu^-\bar{b}\bar{b}$ can be written as a sum over the spin states of the intermediate massive particles of the production times the decay amplitudes for each spin component. In the classical limit there is no interference between these amplitudes. However, in general, these amplitudes do interfere. The size of these interference terms can be used as a measure of how well the classical result for a particular basis describes the full process: if the interference terms are small, then the classical picture captures nearly all of the physics. On the other hand, if the interference terms are large, a significant amount of the physics is omitted from the classical picture.

To quantify these considerations, at each kinematic point for a given process, we may define the quantity $\hat{\mathcal{I}}$, the value of the interference terms for a given spin basis divided by the total $2 \rightarrow 4$ matrix element squared. For a process containing N independent intermediate spin configurations, $\hat{\mathcal{I}}$ can range from $-\infty$ (total destructive interference) to $(N-1)/N$ (total constructive interference). A plot of $d\sigma/d\hat{\mathcal{I}}$ displays the relative importance of the

⁶If charge identification is not available for the b jets, then the distributions presented here should be folded about $\cos \chi_H = 0$.

various values of $\widehat{\mathcal{I}}$. Clearly, in the ideal case where classical intuition captures all of the physics, this distribution will be a delta function centered at $\widehat{\mathcal{I}} = 0$. Fig. 11 compares the helicity, beamline and ZH -transverse bases for ZH production and decay, whereas Fig. 12 does the same for ZZ . For the signal (ZH), we see that the peaking in $\widehat{\mathcal{I}}$ is about an order of magnitude greater in the ZH -transverse basis than in the beamline basis. The helicity basis shows essentially no peaking. For the background (ZZ), the difference is not as dramatic, but it is still clear that the ZH -transverse basis gives the smallest interference terms, and hence the superior description.

E. Pseudoscalar Higgs

Although the Higgs boson of the Standard Model is unambiguously CP -even, for the sake of comparison, it is useful to consider how the spin correlations differ for a CP -odd Higgs A (commonly referred to as a pseudoscalar), a feature of two-doublet Higgs models. Although a tree-level ZZA coupling is forbidden, such a coupling can be generated at the one-loop level [15]. Following Ref. [3], we write the (effective) ZZA vertex as

$$-\frac{igM_Z}{\cos\theta_W}\frac{\eta}{\Lambda^2}k_1^\mu k_2^\nu\varepsilon_{\mu\nu\alpha\beta}, \quad (27)$$

where k_1 and k_2 are the 4-momenta of the two Z 's, η is a dimensionless coupling constant, and Λ is the mass scale at which this vertex is generated. This coupling leads to the differential cross section

$$\frac{d\sigma^\lambda(e^+e^-\rightarrow ZA)}{d(\cos\theta^*)} = \frac{G_F^2 M_W^2}{\cos^2\theta_W} \left(\frac{M_Z}{\Lambda}\right)^4 \frac{\beta_Z^3 \gamma_Z M_Z}{32\pi s^{1/2}} \left(\frac{s + M_Z^2 - M_H^2}{s - M_Z^2}\right)^2 \times \left\{ \cos^2 2\theta_W [\tilde{\mathcal{S}}_L^\lambda(\theta^*, \xi)]^2 + 4 \sin^4 \theta_W [\tilde{\mathcal{S}}_R^\lambda(\theta^*, \xi)]^2 \right\}. \quad (28)$$

In this case the spin functions are independent of energy:

$$\begin{aligned} \tilde{\mathcal{S}}_L^\pm(\beta_Z, \theta^*, \xi) &= \tilde{\mathcal{S}}_R^\mp(\beta_Z, \theta^*, \xi) = \frac{1}{\sqrt{2}}(\cos\theta^* \pm \cos\xi); \\ \tilde{\mathcal{S}}_L^0(\theta^*, \xi) &= \tilde{\mathcal{S}}_R^0(\theta^*, \xi) = \sin\xi \end{aligned} \quad (29)$$

Thus, the total (unpolarized) differential cross section is

$$\sum_\lambda \frac{d\sigma^\lambda}{d(\cos\theta^*)} = \frac{G_F^2 M_W^2}{\cos^2\theta_W} \left(\frac{M_Z}{\Lambda}\right)^4 \frac{\beta_Z^3 \gamma_Z M_Z}{32\pi s^{1/2}} \left(\frac{s + M_Z^2 - M_H^2}{s - M_Z^2}\right)^2 \times (1 - 4\sin^2\theta_W + 8\sin^4\theta_W)(2 - \sin^2\theta^*), \quad (30)$$

in agreement with Ref. [3].

It is clear from the especially simple form of the spin functions, Eq. (29), that the optimal basis for ZA is the helicity basis, independent of the machine energy. Only the helicity basis has the property that one of the three amplitudes (the longitudinal one) vanishes.

Because the ξ dependence of the ZH and ZA amplitudes differs so greatly, a measurement of the Z spin composition of a Higgs signal for different choices of ξ could potentially

differentiate between the two cases. In particular, it would be useful to measure the fraction of longitudinally polarized Z 's in a sample of Z -Higgs candidates in both the helicity and ZH -transverse bases. For the signal events, a scalar Higgs should show no longitudinal Z 's in the ZH -transverse basis, while for a pseudoscalar Higgs this would occur only in the helicity basis.

IV. THE PROCESS $e^+e^- \rightarrow W^+W^-$ AT LEP

A total of three diagrams contribute to the total $e^+e^- \rightarrow W^+W^-$ cross section. We regroup these three diagrams into three contributions as follows. First, we note that the two diagrams involving an s -channel photon or Z boson contribute for both possible chiralities of the initial fermion line. Thus, the first two contributions to the total cross section will be referred to as the $(\gamma/Z)_L$ and $(\gamma/Z)_R$ pieces.⁷ The third diagram involves the t -channel exchange of a neutrino and contributes only when the initial fermion line is left-handed. It will form the third contribution, which we will refer to as the neutrino piece.

Before presenting the differential cross sections for polarized production, let us consider the relative size of these three contributions to the total cross section. In Table IV, we have tabulated the values for each piece at tree-level for a machine energy of 192 GeV. We see that the $(\gamma/Z)_R$ contribution is insignificant. Furthermore, there is a non-trivial interference term, which we will denote by $\text{Inf}[(\gamma/Z)_L, \nu]$, between the $(\gamma/Z)_L$ and neutrino contributions.⁸ In Fig. 13, we have plotted the squares of the three contributions as well as the interference term $\text{Inf}[(\gamma/Z)_L, \nu]$ as a function of the zero momentum frame production angle θ^* , which is taken to be the angle between the momentum of the electron and the W^- . Although it is tempting to attribute the well-known peaking of the cross section in the forward direction to the t -channel pole in the neutrino diagram, Fig. 13 indicates that this is not the case. The square of the neutrino diagram is not only well-behaved near $\cos \theta^* = 1$, but even *decreases* slightly in that region. Instead, the shape of the differential cross section is dominated by the interference between the $(\gamma/Z)_L$ and neutrino pieces, which changes sign from $-$ to $+$ for increasing $\cos \theta^*$. These general features become even more pronounced at higher center-of-mass energies.

⁷From our point of view, the interference between the photon and the Z is trivial in the sense that it shows up as a (W) spin-independent prefactor: no choice of spin basis for the W 's can make these two contributions easier or harder to separate. Note that the contribution from the photon alone may be determined from Eqs. (31) and (32) by taking the Z mass to infinity, and dropping the last term of Eq. (31).

⁸Recall that different helicity amplitudes do not interfere: hence the absence of interference terms between the right-handed (γ/Z) contribution and the left-handed pieces.

A. Polarized Production

To describe the polarized production cross sections for $e^+e^- \rightarrow W^+W^-$, we choose to identify the W^- with particle P_1 and the W^+ with particle P_2 in Fig. 1.

We now present the differential cross sections for polarized W^+W^- production. When the initial fermion pair has left-handed chirality, we have

$$\frac{d\sigma_L^{\lambda\bar{\lambda}}(e\bar{e} \rightarrow W^+W^-)}{d(\cos\theta^*)} = \frac{G_F^2 M_W^2}{256\pi} \beta \gamma^2 \left\{ \frac{2(M_W/M_Z)^2 - (1 - \beta^2) \sin^2\theta_W}{4(M_W/M_Z)^2 - (1 - \beta^2)} [\mathcal{S}_L^{\lambda\bar{\lambda}}(\beta, \theta^*, \xi) - \mathcal{S}_L^{\lambda\bar{\lambda}}(-\beta, \theta^*, \xi)] \right. \\ \left. - \frac{2}{1 - 2\beta \cos\theta^* + \beta^2} \mathcal{S}_L^{\lambda\bar{\lambda}}(\beta, \theta^*, \xi) \right\}^2. \quad (31)$$

Here λ ($\bar{\lambda}$) is the spin of the W^- (W^+). The first term in the curly brackets is the (γ/Z) contribution, while the second term comes from the neutrino. For the other initial fermion chirality (right-handed), we have simply

$$\frac{d\sigma_R^{\lambda\bar{\lambda}}(e\bar{e} \rightarrow W^+W^-)}{d(\cos\theta^*)} = \frac{G_F^2 M_W^2}{256\pi} \frac{\beta}{\gamma^2} \frac{\sin^4\theta_W}{[4(M_W/M_Z)^2 - (1 - \beta^2)]^2} [\mathcal{S}_R^{\lambda\bar{\lambda}}(\beta, \theta^*, \xi) - \mathcal{S}_R^{\lambda\bar{\lambda}}(-\beta, \theta^*, \xi)]^2. \quad (32)$$

All of the spin information is contained in the $\mathcal{S}'s$, which are the same spin functions defined in connection with ZZ production, namely Eqs. (16)–(23). Naturally, we should re-interpret β as the common ZMF speed of the two W 's.

The presence of the neutrino contribution to Eq. (31) makes the expression for the total differential cross section somewhat messy:

$$\sum_{\lambda, \bar{\lambda}, C} \frac{d\sigma_C^{\lambda\bar{\lambda}}}{d(\cos\theta^*)} = \frac{G_F^2 M_W^2}{8\pi} \frac{2(M_W/M_Z)^4 - 2(M_W/M_Z)^2(1 - \beta^2) \sin^2\theta_W + (1 - \beta^2)^2 \sin^4\theta_W}{[4(M_W/M_Z)^2 - (1 - \beta^2)]^2} \\ \times \beta^3 \left\{ 16 + [4\beta^2\gamma^2 + 3(1 - \beta^2)] \sin^2\theta^* \right\} \\ + \frac{G_F^2 M_W^2}{8\pi} \beta \left\{ 2 + \frac{1}{2} \beta^2 \gamma^2 \sin^2\theta^* + \frac{2\beta^2(1 - \beta^2) \sin^2\theta^*}{(1 - 2\beta \cos\theta^* + \beta^2)^2} \right\} \\ - \frac{G_F^2 M_W^2}{8\pi} \frac{2(M_W/M_Z)^2 - (1 - \beta^2) \sin^2\theta_W}{4(M_W/M_Z)^2 - (1 - \beta^2)} \\ \times \beta \left\{ (1 + \beta^2)[4 + \beta^2\gamma^2 \sin^2\theta^*] + \frac{2(1 - \beta^2)[\beta^2 \sin^2\theta^* - 2(1 - \beta^2)]}{1 - 2\beta \cos\theta^* + \beta^2} \right\}. \quad (33)$$

The successive terms in Eq. (33) come from the square of the (γ/Z) contributions (summed over both e^+e^- chiralities), the square of the neutrino contribution, and the interference term $\text{Inf}[(\gamma/Z)_L, \nu]$.

As in the ZZ case, the individual spin-dependent amplitudes are complicated. Therefore, in Fig. 14, we have plotted the fractional contribution to each of the six independent spin configurations for a center-of-mass energy of 192 GeV. From these plots, we see that the $[(++) + (--)]$ and (00) contributions never dominate the total amplitude at 192 GeV, while the $[(+0) + (0-)]$ or $(+-)$ contributions can be made large with the proper choice of ξ .

B. Spin Bases

From the contour plots and the expressions for the spin components we have identified four interesting spin bases: helicity, $(+-)$ -maximized, beamline, and $[(+0) + (0-)]$ -maximized, which we have studied in some detail. In Fig. 15, we have plotted the connection between ξ and θ^* at 192 GeV for these four bases. In Tables V–VIII, we indicate the fraction of the total cross section, (γ/Z) , ν and $\text{Inf}[(\gamma/Z)_L, \nu]$ contributions broken down into the six independent spin configurations for an e^+e^- collider running at 192 GeV.

We begin our survey with the helicity basis. This basis has one noteworthy feature: the $(+-)$ and $(-+)$ components of both (γ/Z) contributions vanish at all \sqrt{s} . This is not true for the neutrino diagram; therefore, a measurement of these spin components is a direct measurement of the neutrino contribution. At $\sqrt{s} = 192$ GeV the sum of these two spin components is 56% of the total cross section.

Another useful basis is the $(+-)$ -maximized basis, which is defined by choosing ξ so that the $(+-)$ component is as large as possible. In principle, it is a straightforward exercise to derive an analytic expression connecting ξ and θ^* by differentiating $d\sigma^{+-}/d(\cos \theta^*)$ with respect to ξ and setting the result equal to zero. In practice, however, such an expression would be too complicated to be illuminating. Furthermore, it turns out that we must allow negative values of $\sin \xi$ in order to get the largest possible contribution. This is equivalent examining both the $(+-)$ and $(-+)$ amplitudes, and taking the larger of the two at each point. Selecting $\sin \xi < 0$ whenever the $(-+)$ amplitude is chosen converts it to a $(+-)$ amplitude, according to Eq. (21). Thus, it is expedient to use a numerical procedure to determine ξ in this basis: the results are plotted in Fig. 15 for $\sqrt{s} = 192$ GeV. The discontinuity seen in the $\cos \xi$ versus $\cos \theta^*$ curve for this basis near $\cos \theta^* = -0.8$ is caused by the presence of two competing maxima. At $\sqrt{s} = 192$ GeV the $(+-)$ component is 64% of the total in this basis.

In the beamline basis, defined by Eq. (2), the direction of the spin axis for the W^- (W^+) viewed in its rest frame coincides with the direction of the electron (positron) in that frame. With the choice (2) for ξ , the functions $\mathcal{G}_1(\beta, \theta^*, \xi + \pi)$ and $\mathcal{G}_3(\beta, \theta^*, \xi)$ vanish. This means that the neutrino does not contribute to the $[(++) + (--)]$, $[(0+) + (0-)]$, and $(-+)$ spin configurations [16]. Unfortunately, the fraction of the total in these spin configurations is small, less than 5% at $\sqrt{s} = 192$ GeV. However, the $[(+0) + (0-)]$ component is 80% of the total at this \sqrt{s} .

Finally, we come to the $[(+0) + (0-)]$ -maximized basis, which is defined by choosing the value of ξ which maximizes the fraction of the amplitude coming from the $[(+0) + (0-)]$ component. Once again the maximization condition leads to a complicated expression (it is a quartic equation for $\tan \xi$). Therefore, we present the numerically derived solution in Fig. 15. In this basis, the $[(+0) + (0-)]$ component is more than 92% of the total at $\sqrt{s} = 192$

GeV.

For these last three bases, $(+-)$ -maximized, beamline, and $[(+0) + (0-)]$ -maximized, there are large negative interference terms between the ν and $(\gamma/Z)_L$ contributions in all of the dominant spin components.

Fig. 16 shows the angular dependence of the polarized production cross sections. It is clear from these plots that in the helicity basis, there is a complicated structure, with four different amplitudes being the largest, depending on the value of $\cos \theta^*$. On the other hand, in the $(+-)$ -maximized basis, the $(+-)$ component dominates at all angles. Likewise, in the beamline and $[(+0) + (0-)]$ -maximized bases, the $[(+0) + (0-)]$ component dominates at all angles.

Finally, because the relative contributions of the polarized cross sections depend upon the center-of-mass energy, we display this dependence in the range from threshold to 210 GeV in Fig. 17. As mentioned near the end of Sec. III A, the effect of including initial state radiation in the results is to produce events at lower \sqrt{s} . From Fig. 17, we see that the addition of such events would slightly increase the fraction of the dominant spin component in the beamline and $[(+0) + (0-)]$ -maximized bases and slightly decrease the dominant component in the helicity and $(+-)$ -maximized bases. The $[(+0) + (0-)]$ -maximized basis is slightly less sensitive to small shifts in \sqrt{s} than the beamline basis, while the $(+-)$ -maximized basis is slightly less sensitive to small shifts in \sqrt{s} than the helicity basis.

C. Polarized Decay

The presence of maximal parity violation in the coupling between the W boson and fermions results in distinctly different angular distributions for the W decay products for all three W polarizations. In fact, the decay distributions in the rest frame of the decaying W^- (or W^+) are the same as for Z decay [*i.e.* Eqs. (25) and (26)] with $\alpha_f = 1$ for all possible final states, leptonic and hadronic. Thus, they follow the $\nu\bar{\nu}$ curves presented in Fig. 8. Note, however, in the case of $W^+ \rightarrow \ell\nu$, it is more convenient to use the distribution in the *antilepton* angle $\bar{\chi}$: this distribution may be generated by replacing $\cos \chi$ with $-\cos \bar{\chi}$ in Eqs. (25) and (26).

Because the distributions for transversely-polarized W 's are narrower than the one for longitudinally-polarized W 's, it is easier to identify the $+$ and $-$ polarization states than the 0 state. To demonstrate this, suppose we “tag” the spin of the parent W^- based on the value of $\cos \chi$ as follows: the spin is taken to be $+$ if $\cos \chi < -y$, $-$ if $\cos \chi > y$, and 0 if $|\cos \chi| \leq y$. The probabilities that these assignments are correct may be computed from Eqs. (25) and (26), yielding

$$\begin{aligned} \frac{1}{12}(7 + 4y + y^2), & \quad \pm \text{ states} \\ \frac{1}{6}(3 - y^2), & \quad 0 \text{ state.} \end{aligned} \tag{34}$$

No matter what value is chosen for y , the probability of correct identification in the central region is always less than 50%. On the other hand, the correct identification rate for the $+$ and $-$ states in their respective regions can be of order 75%.

D. Correlations

We now consider correlations between the decay products of the W^+W^- pair. For the sake of concreteness, let us consider the case where the W^- decays to $\mu^-\bar{\nu}_\mu$ and the W^+ decays to $\mu^+\nu_\mu$. Let χ be the angle between the μ^- emission direction and the W^- spin axis in the W^- rest frame, and $\bar{\chi}$ be the angle between the μ^+ emission direction and the W^+ spin axis in the W^+ rest frame. For simplicity we are assuming one can determine the direction of the two neutrinos. If one of the W -bosons decays into two jets, then the correlations of the down-quark jet are the same as that of the charged lepton. Since determining which jet is the down-type jet is problematic, the distributions given here will have to be folded such that they are symmetric when $\cos \chi \leftrightarrow -\cos \chi$.

The first set of correlations we wish to discuss may be conveniently displayed as a scatter plot in $\cos \chi$ and $\cos \bar{\chi}$. In Fig. 18 we have plotted the predictions for this distribution using the helicity, $(+-)$ -maximized, beamline, and $[(+0) + (0-)]$ -maximized bases. On one hand, the $[(+0) + (0-)]$ -maximized plot is very nearly the pure distribution for the decay of the $[(+0) + (0-)]$ spin state. However, the broadness of the decay distributions for the longitudinal W 's cause the events to be rather spread out in this plot. On the other hand, there is a nice contrast between the maximum and minimum values in the $(+-)$ -maximized plot. The functional dependence is less simple, however, as fully three of the six spin configurations contribute at or above the 10% level.

Although a precision measurement of the complete 2-dimensional distribution requires a large number of events, it is still possible to perform some interesting tests with fewer events. For example, if CP is conserved, then the scatter plot will be symmetric about the line $\cos \chi = \cos \bar{\chi}$. So a measure of the asymmetry in the number of events on either side of this line provides a simple test of CP symmetry.

In Fig. 19, we have plotted the distribution of the interference terms $d\sigma/d\hat{\mathcal{I}}$ (as described in Sec. III D) for W^+W^- production and decay using the helicity, $(+-)$ -maximized, beamline, and $[(+0) + (0-)]$ -maximized bases. None of the bases under consideration (nor any basis which we have found) performs particularly well in this respect. The $(+-)$ -maximized basis contains the smallest interference terms on average, but there is still a non-negligible component away from $\hat{\mathcal{I}} = 0$. This bump/peak at positive $\hat{\mathcal{I}}$ for all spin bases is caused by the strong azimuthal correlations associated with the pure $V-A$ coupling of the W -boson to its decay products. A similar structure appears in the $\hat{\mathcal{I}}$ plots for $e^+e^- \rightarrow ZZ$ in the situation where both Z 's decay to $\nu\bar{\nu}$.

Although there is no obvious spin basis which is ideally suited to the study of W pair production at LEP, the $(+-)$ -maximized basis is clearly better than the helicity basis in many ways. The same can be said of the $[(+0) + (0-)]$ -maximized basis compared to the beamline basis. A detailed study of the correlations in more than one basis is required to disentangle the spin correlations in this process.

V. CONCLUSIONS

If the Higgs mass turns out to be in the vicinity of the Z mass, then the ZH -transverse basis, in which the Z produced in association with the Higgs is purely in the \pm polarization

states, provides a useful handle with which to distinguish between ZH and ZZ events, based upon the angular distributions of the decay products. In this situation, the helicity basis supplies no useful information. Even if the Higgs mass is significantly different from the Z mass, the ZH -transverse basis still exists and leads to distinctive angular correlations among the decay products. A comparison between the ZH -transverse and helicity descriptions of the data is useful for distinguishing a scalar from pseudoscalar Higgs.

For the study of the WW events there is no ideal basis. However, the $(+-)$ -maximized basis is better than helicity, and the $[(+0) + (0-)]$ -maximized basis is better than the beamline basis at describing the correlations. Not only is there a greater fraction of the total cross section concentrated in the dominant components in these preferred bases, but the interference distributions are somewhat narrower. The lack of an ideal basis implies that study of the WW system is best carried out using more than one basis, depending upon which quantity is being tested. Furthermore, simply checking to see that the correlations change in the correct manner as the basis is varied tests the Standard Model in ways which cannot be accomplished with the helicity basis alone.

ACKNOWLEDGMENTS

The Fermi National Accelerator Laboratory (FNAL) is operated by Universities Research Association, Inc., under contract DE-AC02-76CHO3000 with the U.S. Department of Energy. High energy physics research at McGill University is supported in part by the Natural Science and Engineering Research Council of Canada. We would like to thank Peter Fisher and Philip Bambade for illuminating discussions. GM would like to thank the FNAL theory group for their kind hospitality during visits to initiate and wrap-up this work. SP would like to thank the Aspen Center for Physics where a portion of this work was completed.

APPENDIX: POLARIZATION VECTORS FOR MASSIVE VECTOR BOSONS

Following Kuijf [17], we consider a massive vector boson of momentum V and mass M such that $V^2 = M^2$. Let S be the spin vector associated with this vector boson such that $S^2 = -1$ and $V \cdot S = 0$. We need the three polarization vectors ϵ_λ^μ such that in the vector boson rest frame the boson has spin projection $\lambda = (+, 0, -)$ with rest to the spatial part of the spin vector S .

These three polarization vectors are conveniently written in terms of the two vectors

$$V_1 = \frac{1}{2}(V + MS) \quad \text{and} \quad V_2 = \frac{1}{2}(V - MS). \quad (\text{A1})$$

Note $V_1 + V_2 = V$, $V_1^2 = V_2^2 = 0$ and $2V_1 \cdot V_2 = M^2$. The decay products of a transverse vector boson are directly correlated with V_1 and V_2 , not V and S . Using the spinor notation of Mangano and Parke [18], where

$$\langle V_1 \pm | \equiv \bar{u}(V_1) \frac{1}{2}(1 \mp \gamma_5) \quad \text{and} \quad |V_1 \pm \rangle \equiv \frac{1}{2}(1 \pm \gamma_5)v(V_1), \quad (\text{A2})$$

we have

$$\epsilon_\pm^\mu = \frac{\langle V_1 \pm | \gamma^\mu | V_2 \pm \rangle}{\sqrt{2}M} \quad (\text{A3})$$

$$\epsilon_0^\mu = \frac{\langle V_1 + | \gamma^\mu | V_1 + \rangle - \langle V_2 + | \gamma^\mu | V_2 + \rangle}{2M} \left(= \frac{V_1^\mu - V_2^\mu}{M} \right). \quad (\text{A4})$$

The phase factors have been chosen such that ϵ_0^μ is real, $\epsilon_-^\mu = (\epsilon_+^\mu)^*$, and $\epsilon_-^\mu \leftrightarrow \epsilon_+^\mu$ if we interchange V_1 and V_2 . Our convention is that these polarization vectors are for outgoing vector bosons whereas for incoming vector bosons we use $(\epsilon_\lambda^\mu)^*$.

These polarization vectors satisfy transversality, orthogonality, and completeness relations:

$$V \cdot \epsilon_\lambda = 0, \quad (\text{A5})$$

$$\epsilon_\lambda \cdot \epsilon_{\lambda'}^* = -\delta_{\lambda\lambda'}, \quad (\text{A6})$$

$$\sum_\lambda \epsilon_\lambda^\mu \epsilon_{\lambda'}^* = -g^{\mu\nu} + \frac{V^\mu V^\nu}{M^2}. \quad (\text{A7})$$

The helicity basis is obtained by choosing the spatial part of the spin vector S to be in the same direction as the spatial part of the momentum vector V of the vector boson. For example, if

$$V = \gamma M(1, \beta \hat{n}) \quad (\text{A8})$$

using an obvious notation then choose

$$V_1 = \frac{1}{2}\gamma M(1 + \beta)(1, \hat{n}) \quad \text{and} \quad V_2 = \frac{1}{2}\gamma M(1 - \beta)(1, -\hat{n}). \quad (\text{A9})$$

REFERENCES

* Electronic address: mahlon@hep.physics.mcgill.ca

† Electronic address: parke@fnal.gov

- [1] G. Altarelli, T. Sjöstrand and F. Zwirner, eds., *Physics at LEP2*, CERN 96-01, Vol. 1.
- [2] J.D. Bjorken, Proc. Summer Institute on Particle Physics, SLAC Report 198 (1976); J. Ellis, M.K. Gaillard, and D.V. Nanopoulos, Nucl. Phys. **B106**, 292 (1976); B.W. Lee, C. Quigg, and H.B. Thacker, Phys. Rev. **D16**, 1519 (1977); B.L. Ioffe and V.A. Khoze, Sov. J. Part. Nucl. **9**, 50 (1978).
- [3] V. Barger, K. Cheung, A. Djouadi, B.A. Kniehl, and P.M. Zerwas, Phys. Rev. **D49**, 79 (1994).
- [4] J.F. Gunion and Z. Kunszt, Phys. Rev. **D33**, 665 (1986).
- [5] K. Hagiwara, R.D. Peccei, D. Zeppenfeld and K. Hikasa, Nucl. Phys. **B282**, 253 (1987).
- [6] K.J.F. Gaemers and G.J. Gounaris, Z. Phys. **C1**, 259 (1979); G. Gounaris, J. Layssac, G. Moultsaka, and F.M. Renard, Int. J. Mod. Phys. **A8**, 3285 (1993); M. Bilenky, J.L. Kneur, F.M. Renard, and D. Schildknecht, Nucl. Phys. **B409**, 22 (1993); K. Hagiwara, T. Hatsukano, S. Ishihara and R. Szalapski, Nucl. Phys. **B496**, 66 (1997).
- [7] G. Mahlon and S. Parke, Phys. Rev. **D53**, 4886 (1996).
- [8] S. Parke and Y. Shadmi, Phys. Lett. **B387**, 199 (1996).
- [9] G. Mahlon and S. Parke, Phys. Lett. **B411**, 173 (1997).
- [10] For a recent review of trilinear gauge boson couplings see: H. Aihara, *et. al.*, in: *Electroweak Physics and Beyond the Standard Model*, World Scientific Publishing Co., Singapore, eds. T. Barklow, S. Dawson, H. Haber, and J. Siegrist, hep-ph/9503425.
- [11] R.M. Barnett et al., Phys. Rev. **D54**, 1 (1996).
- [12] N. Brown, Z. Phys. **C49**, 657 (1991).
- [13] Z. Kunszt and W.J. Stirling, Phys. Lett. **B242**, 507 (1990).
- [14] D.J. Summers, Phys. Lett. **B274**, 209 (1992).
- [15] J. Gunion, H. Haber, G. Kane, and S. Dawson, *The Higgs Hunter's Guide*, Addison-Wesley, Redwood City, CA, 1990.
- [16] M. Pundurs, Z. Phys. **C52**, 449 (1991).
- [17] J.G.M. Kuijf, “Multiparton Production at Hadron Colliders,” Ph.D. Thesis (Leiden University, 1991).
- [18] M. Mangano and S. Parke, Phys. Rep. **200**, 301 (1991).

FIGURES

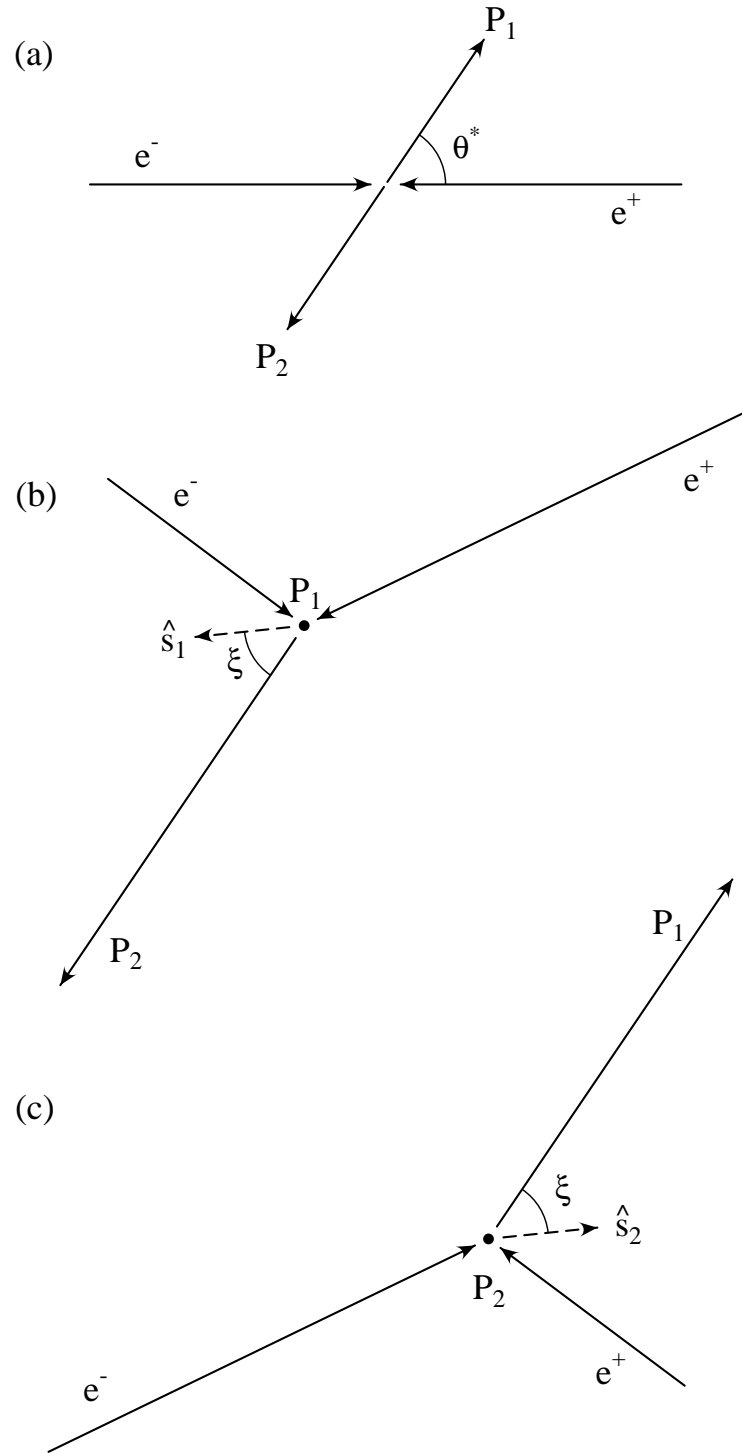


FIG. 1. The scattering process in (a) the zero momentum frame, (b) the rest-frame of P_1 and (c) the rest-frame of P_2 . \hat{s}_j is the spin axis for P_j .

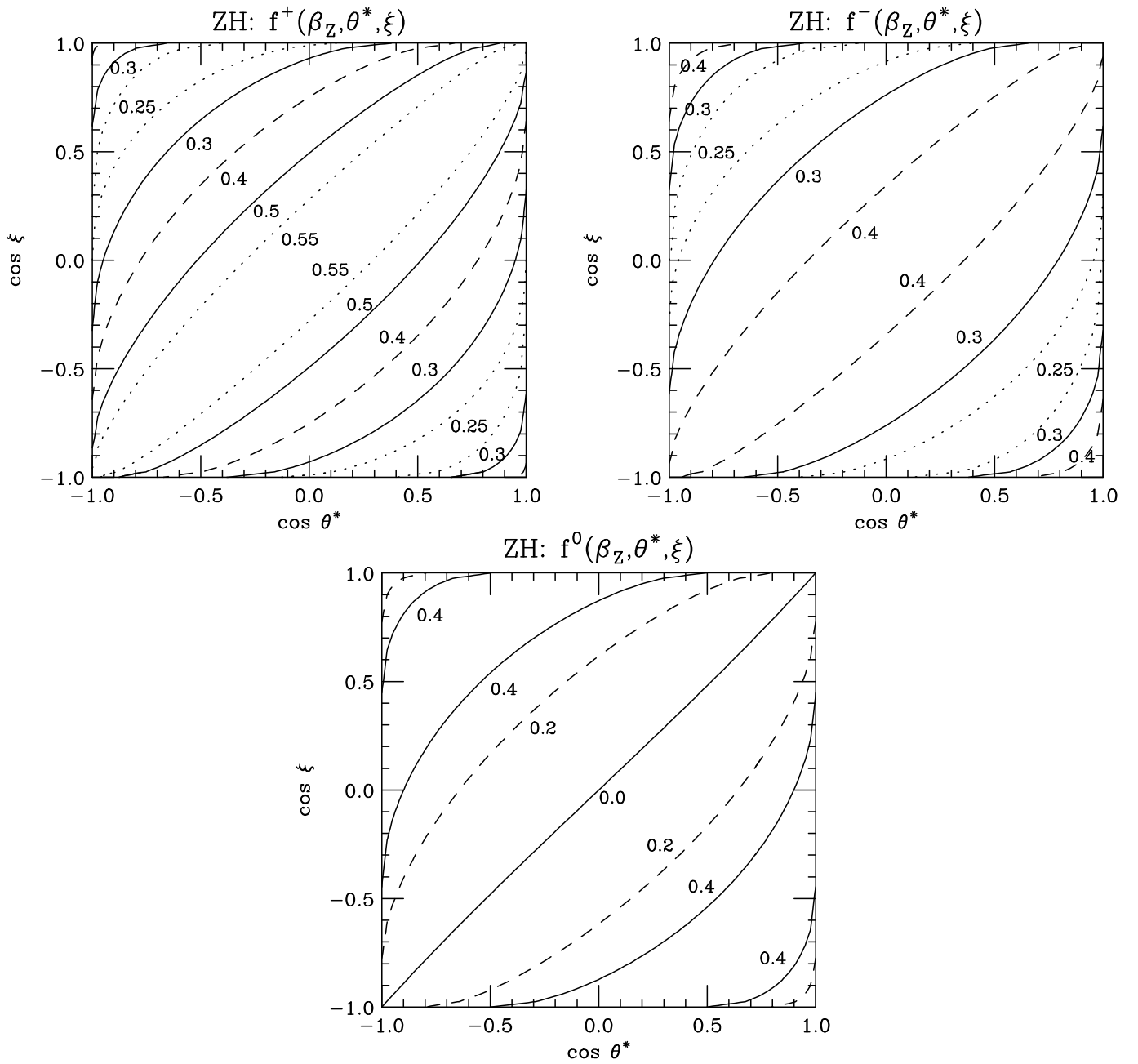


FIG. 2. Structure of the $e^+e^- \rightarrow ZH$ polarized production amplitudes in the $\cos \theta^*$ - $\cos \xi$ plane for $\sqrt{s} = 192$ GeV and $M_H = M_Z$ ($\beta_Z = 0.313$). Plotted is $f^\lambda(\beta_Z, \theta^*, \xi)$, the fraction of the total amplitude squared in each spin configuration [see Eq. (8)]. In all of the plots, $\sin \xi \geq 0$.

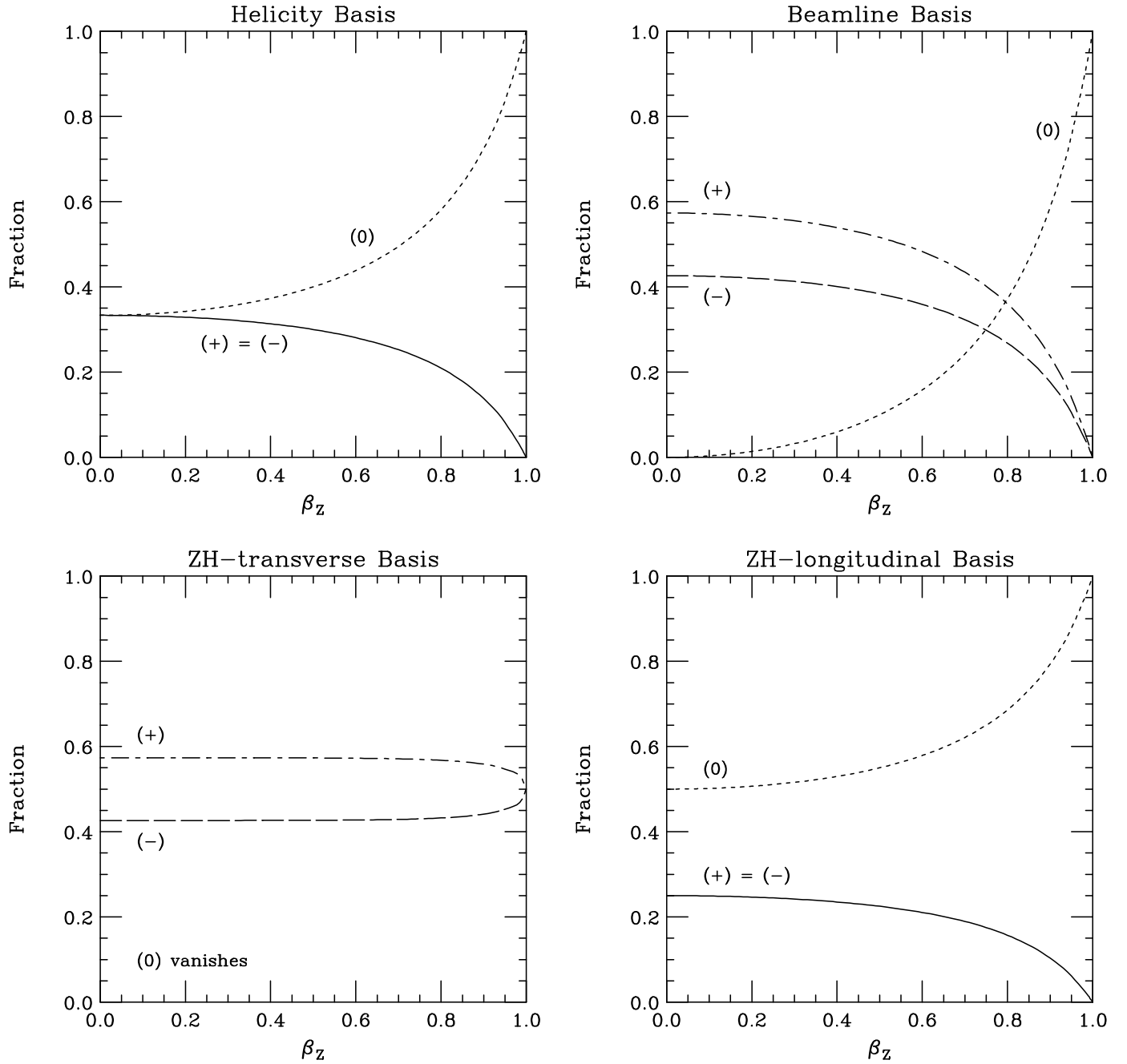


FIG. 3. Spin decomposition of the $e^+e^- \rightarrow ZH$ cross section as a function of the ZMF speed β_z of the Z boson, assuming that $M_H = M_Z$. Shown are the fractions of the total cross section in the $(+)$, $(-)$, and (0) spin states for the helicity, beamline, ZH -transverse, and ZH -longitudinal bases.

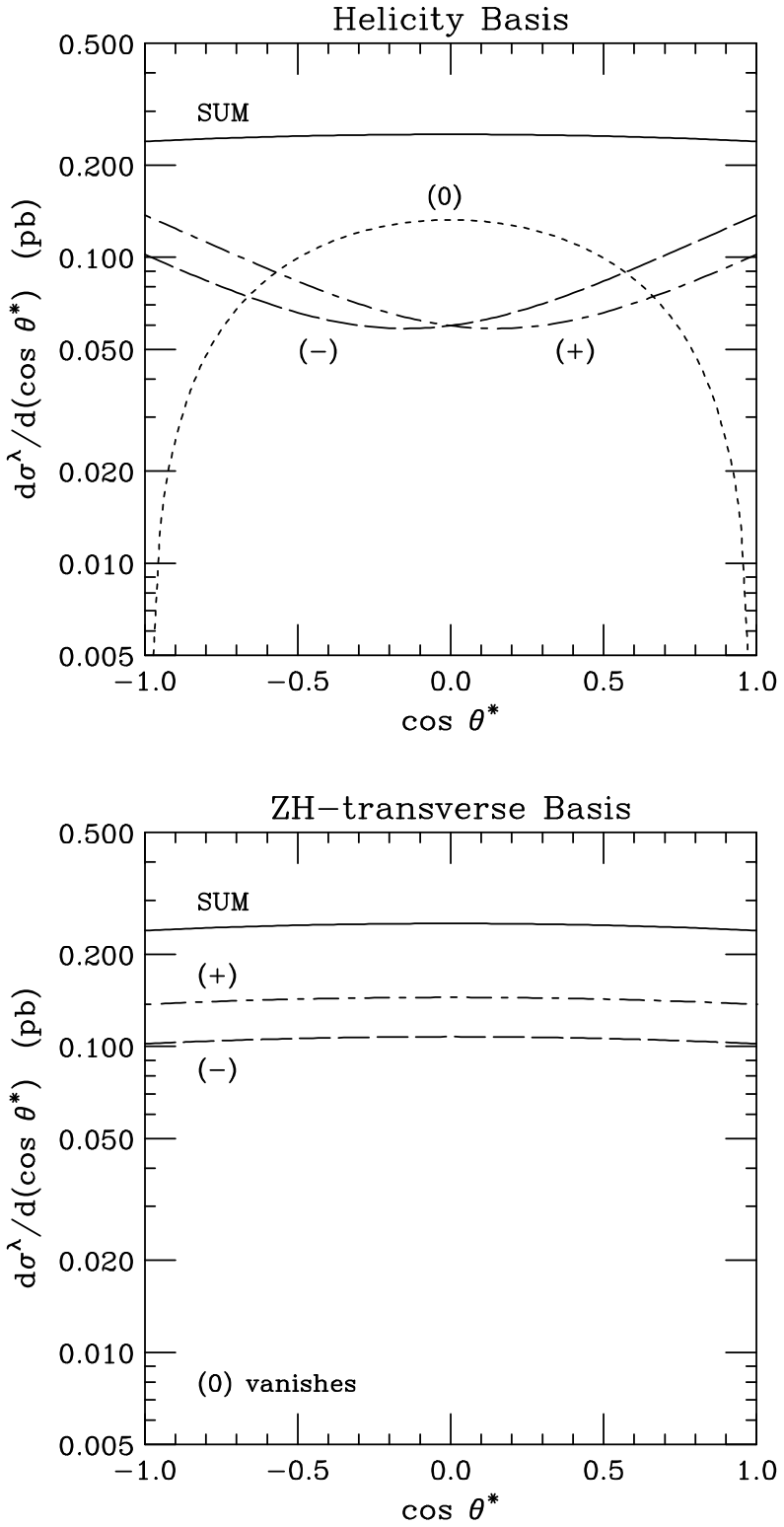


FIG. 4. Distribution in production angle of the $e^+e^- \rightarrow ZH$ cross section for $M_H = M_Z$ at $\sqrt{s} = 192$ GeV, broken down into the contributions from the three possible Z spins, for the helicity and ZH -transverse bases.

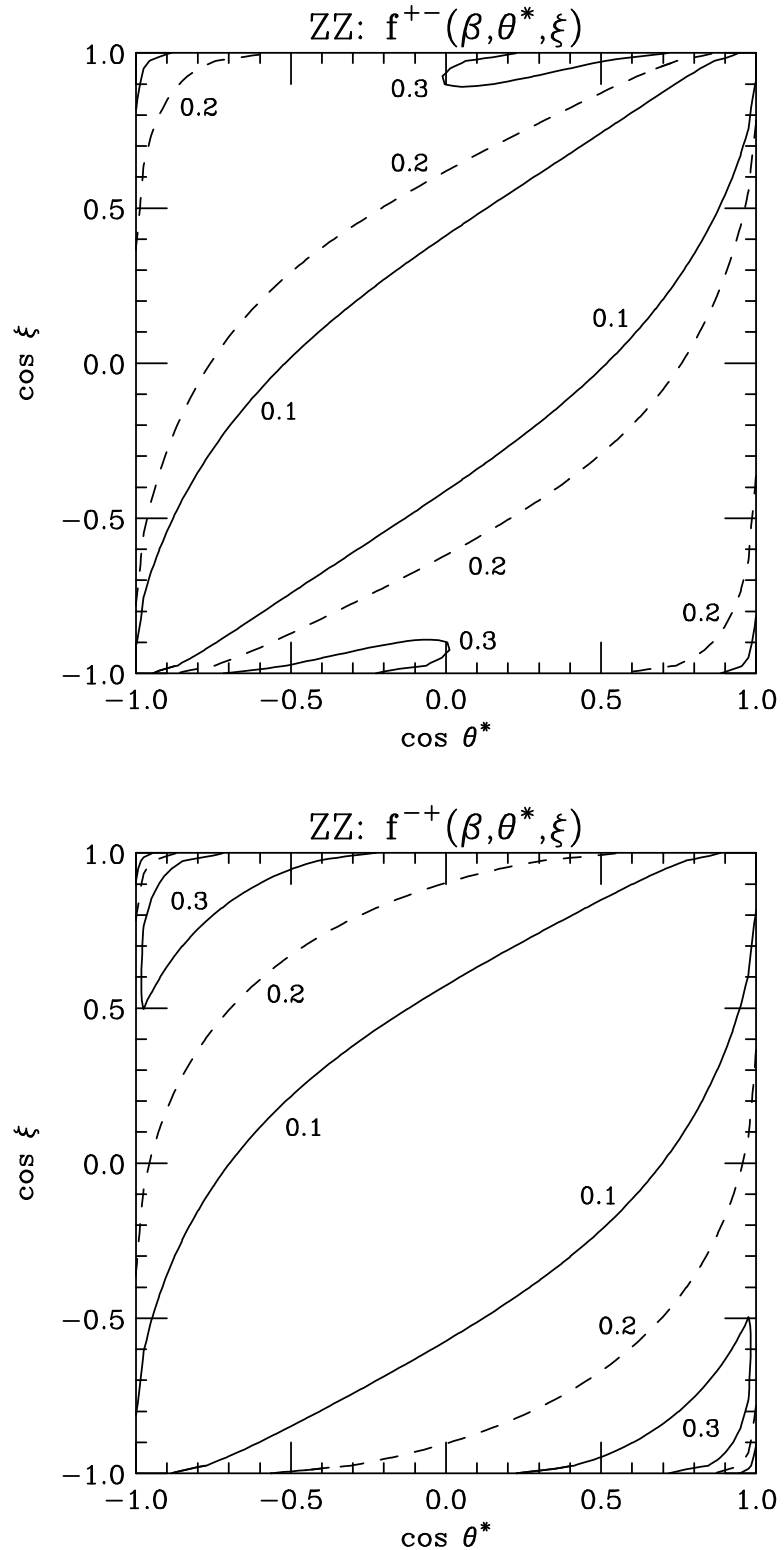


FIG. 5. Structure of the $e^+e^- \rightarrow ZZ$ polarized production amplitudes in the $\cos \theta^*$ - $\cos \xi$ plane for $\sqrt{s} = 192$ GeV ($\beta = 0.313$). Plotted is $f^{\lambda\bar{\lambda}}(\beta, \theta^*, \xi)$, the fraction of the total amplitude squared in each spin configuration [see Eq. (24)]. In all of the plots, $\sin \xi \geq 0$.

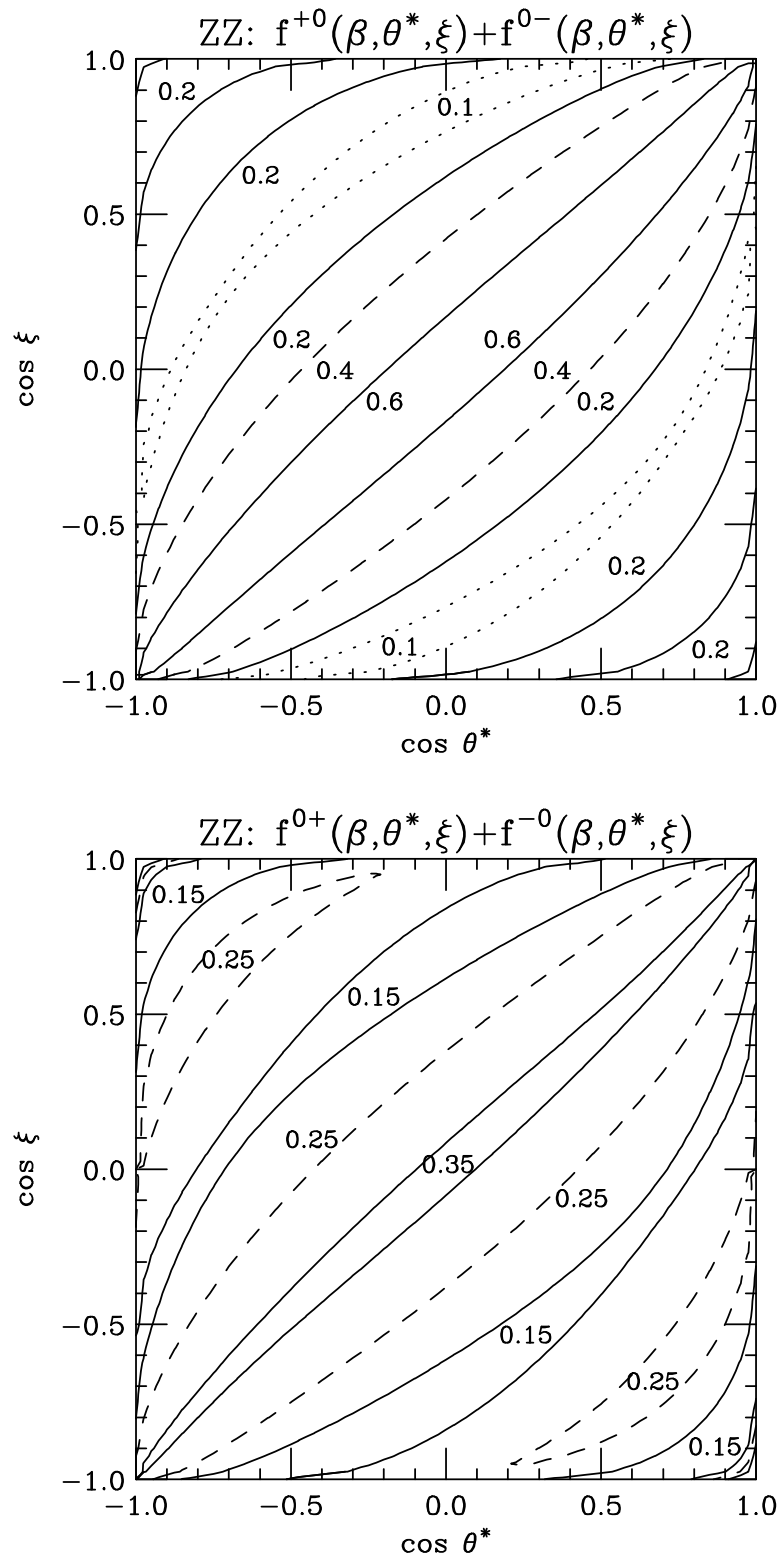


FIG. 5. (continued)

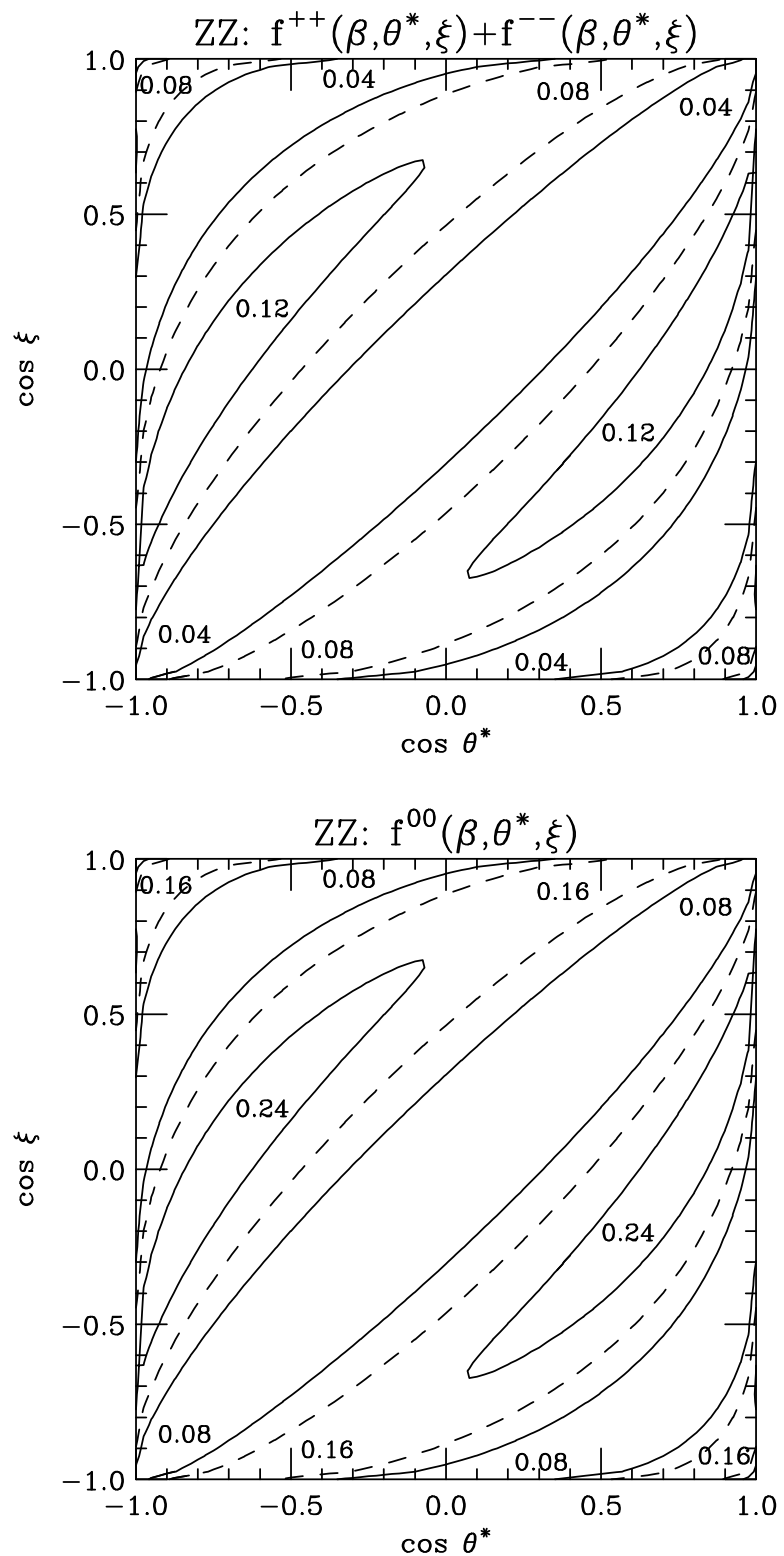


FIG. 5. (continued)

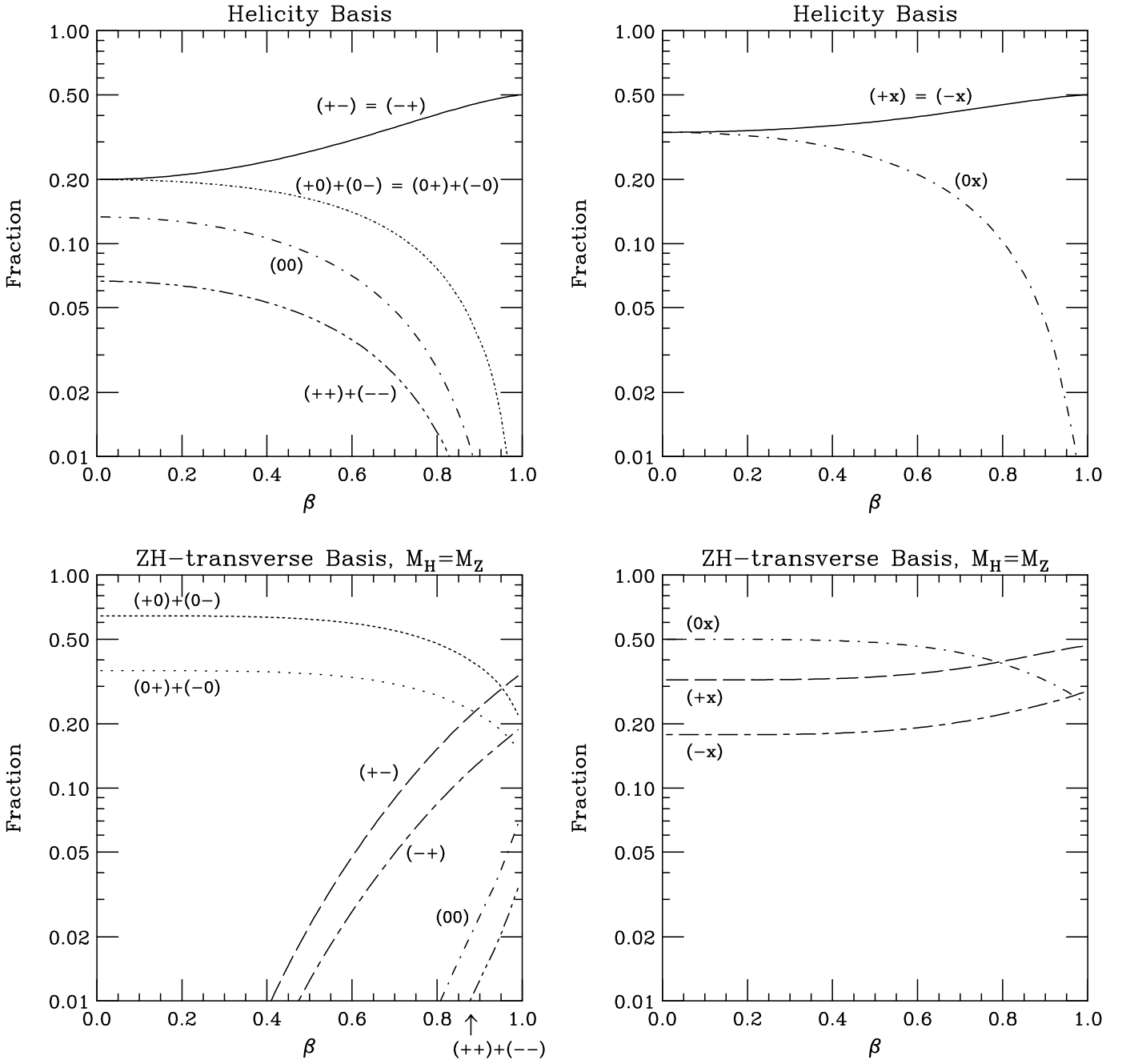


FIG. 6. Spin decomposition of the $e^+e^- \rightarrow ZZ$ cross section as a function of the ZMF speed β of the Z boson. The plots on the left show the fractions of the total cross section in the (00) , $(+-)$, $(-+)$, $[(+0)+(0-)]$, $[(0+)+(-0)]$, and $[(++)+(-)]$ spin states for the helicity and ZH -transverse bases. The plots on the right show inclusive fractions where we have summed over all possible spins of the other Z , *e.g.* $(0x) \equiv (0+) + (00) + (0-)$. The curves for the ZH -transverse basis are drawn for the case $M_H = M_Z$.

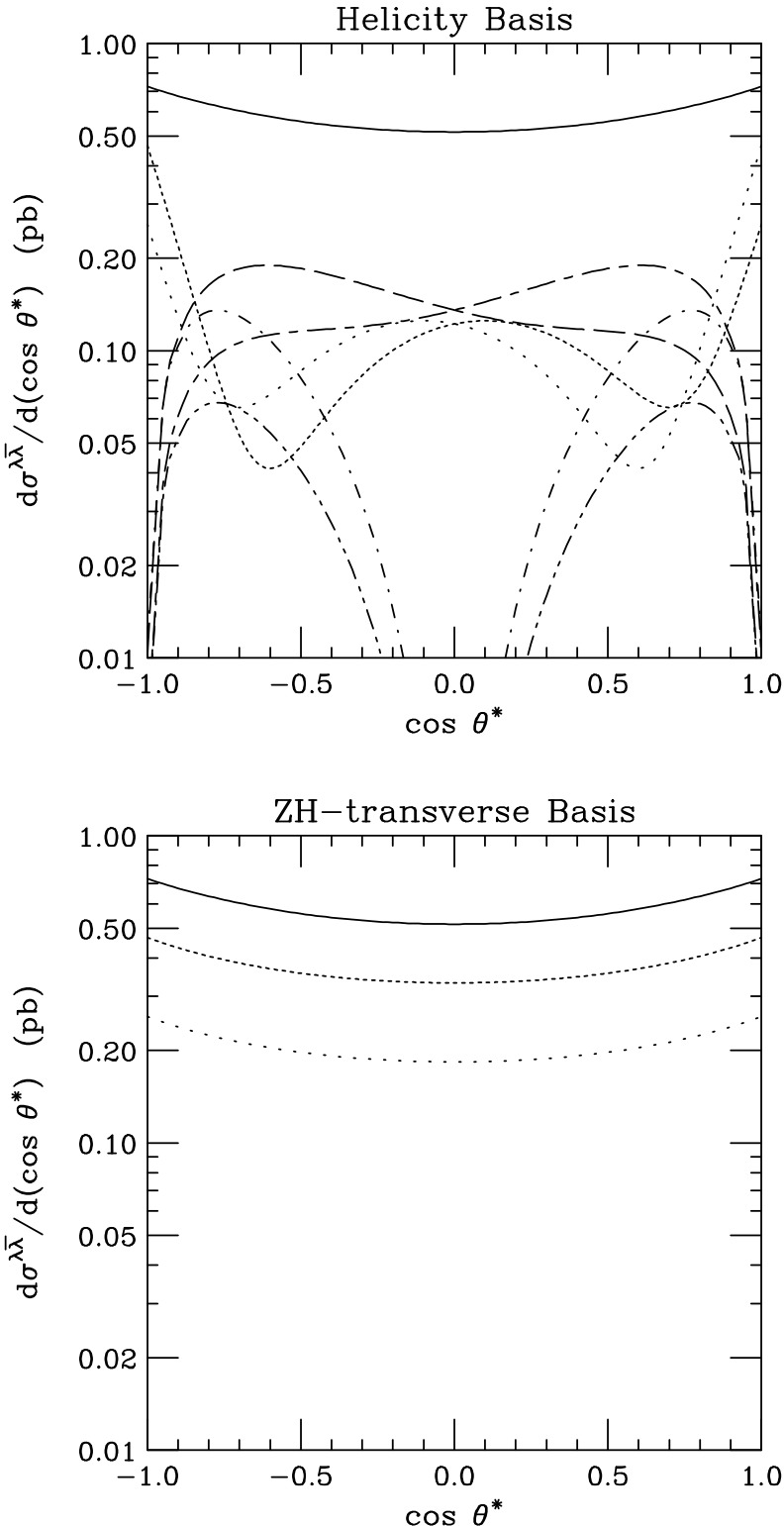


FIG. 7. Distribution in production angle of the $e^+e^- \rightarrow ZZ$ cross section at $\sqrt{s} = 192$ GeV, broken down into the six independent spin combinations for the helicity and ZH -transverse (with $M_H = M_Z$) spin bases. Only two spin components contribute above the 1% level in the ZH -transverse basis.

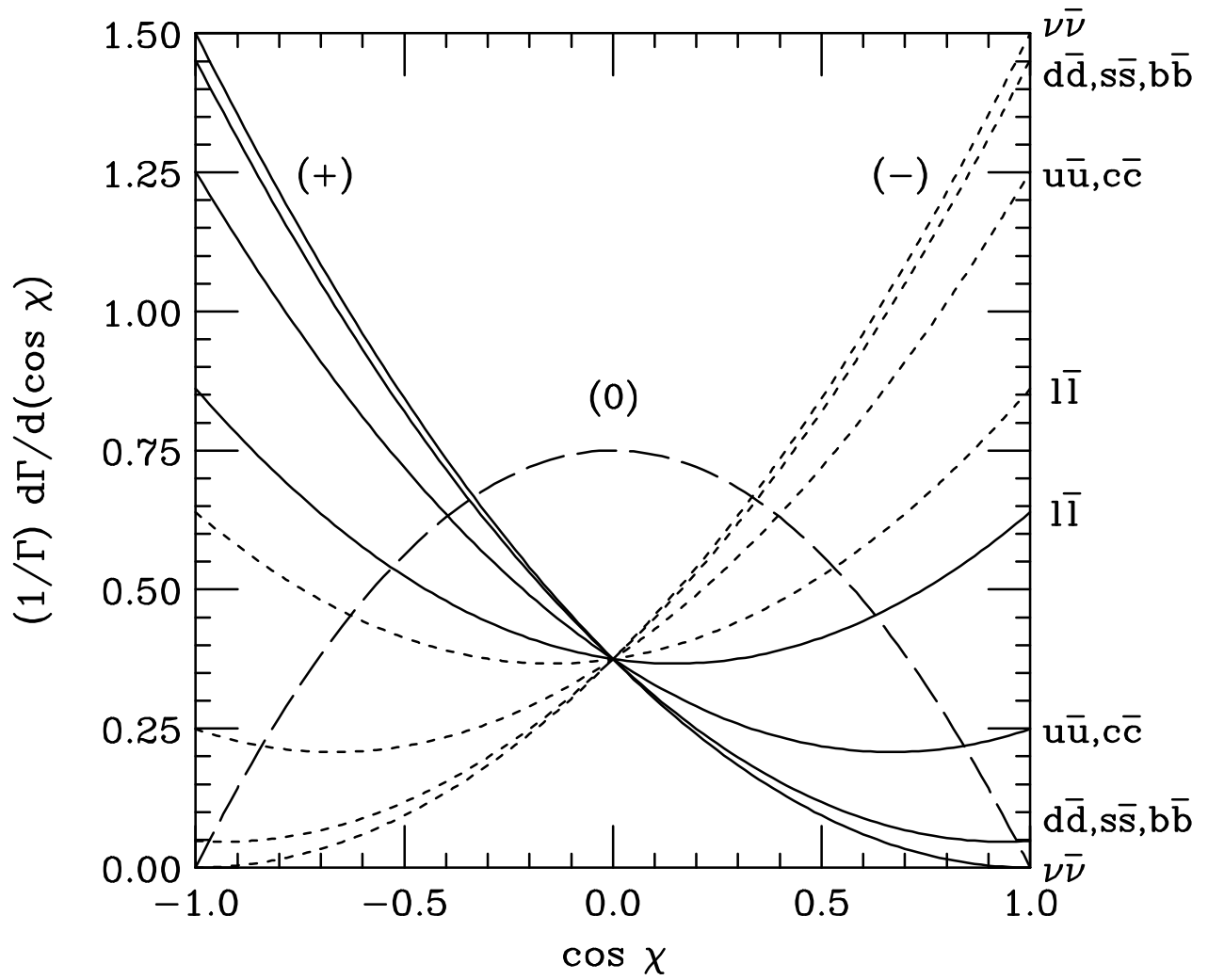


FIG. 8. Angular distributions for the decay of a polarized Z . χ is the angle between the direction of the fermion ($\nu, e, \mu, \tau, u, d, s, c$, or b) and the chosen spin axis, as viewed in the Z rest frame.

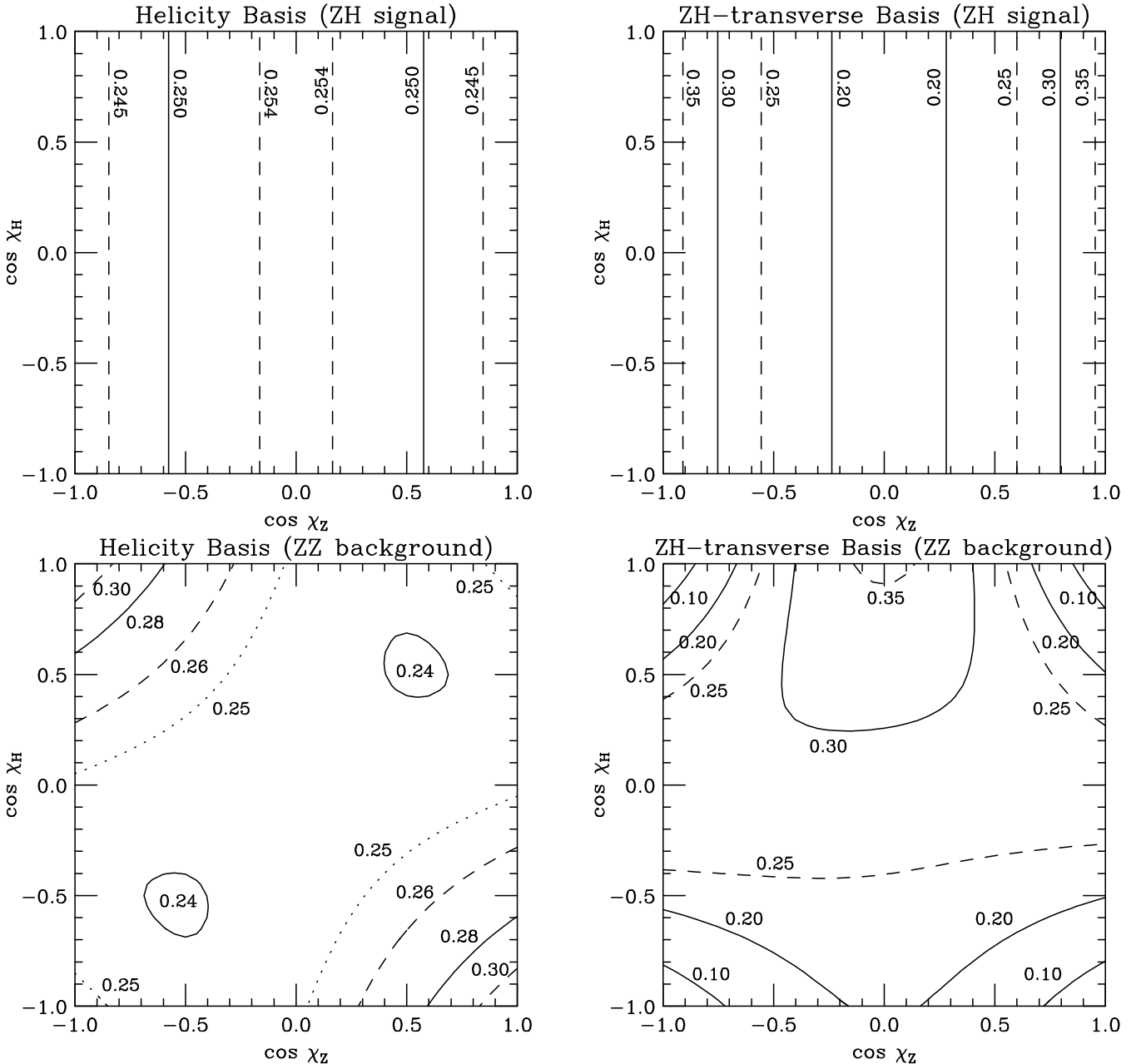


FIG. 9. Double differential decay distributions $(1/\sigma) d^2\sigma/[d(\cos \chi_Z)d(\cos \chi_H)]$ for the processes $e^+e^- \rightarrow ZH/ZZ \rightarrow \ell\bar{\ell}b\bar{b}$ in the helicity and ZH -transverse bases, using $M_H = M_Z$. χ_Z (χ_H) is the angle between the lepton (b jet) and the spin axis, as viewed in the $\ell\bar{\ell}$ ($b\bar{b}$) rest frame. In the absence of charge identification for the b 's, these plots should be folded about $\cos \chi_H = 0$. For completely uncorrelated decays, this distribution would have a uniform value of $1/4$.

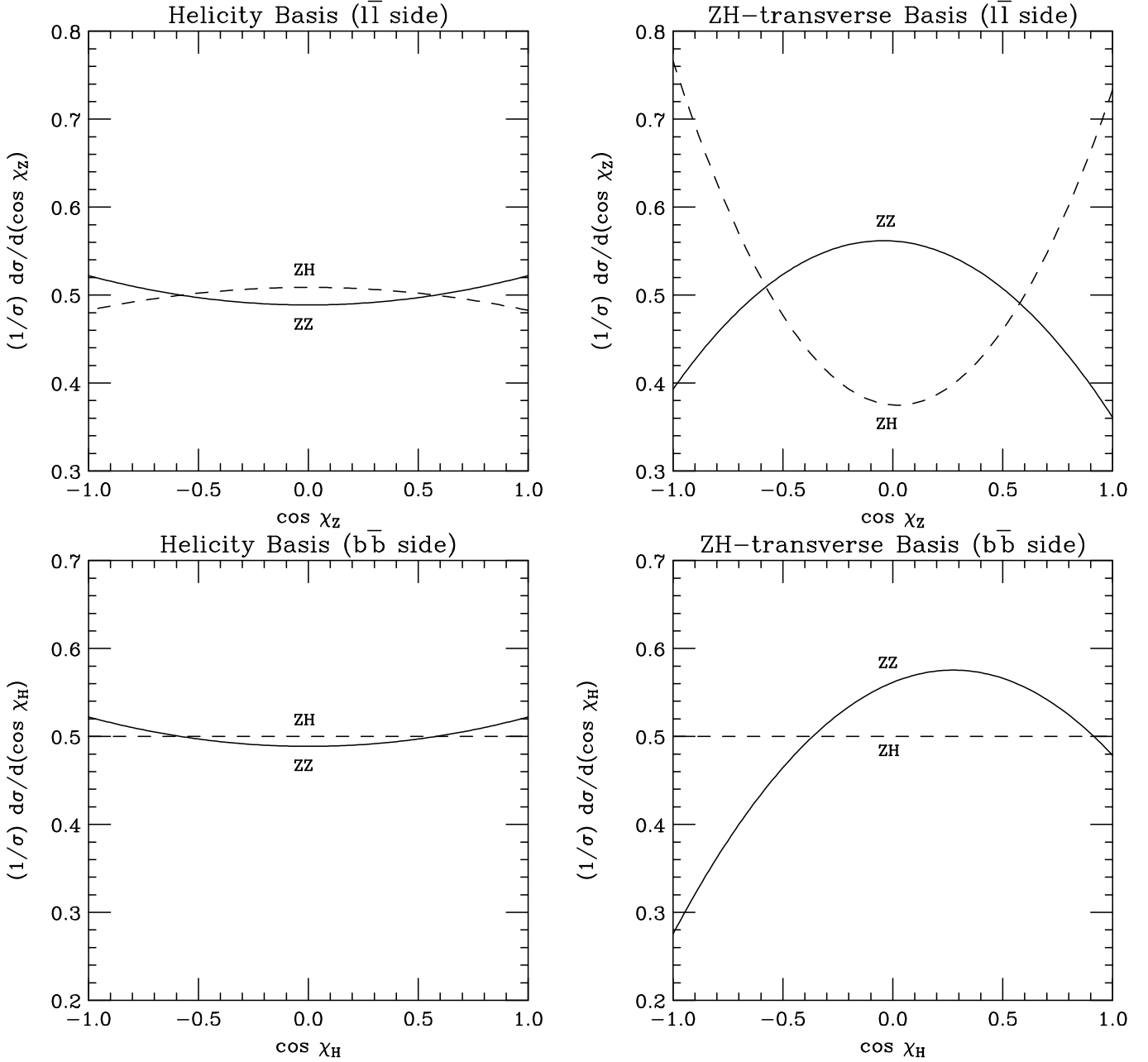


FIG. 10. One dimensional differential decay distributions for the processes $e^+e^- \rightarrow ZH/ZZ \rightarrow \ell\bar{\ell}bb$ in the helicity and ZH -transverse bases, using $M_H = M_Z$. χ_Z (χ_H) is the angle between the lepton (b jet) and the spin axis, as viewed in the $\ell\bar{\ell}$ (bb) rest frame. In the absence of charge identification for the b 's, these plots should be folded about $\cos \chi_H = 0$.

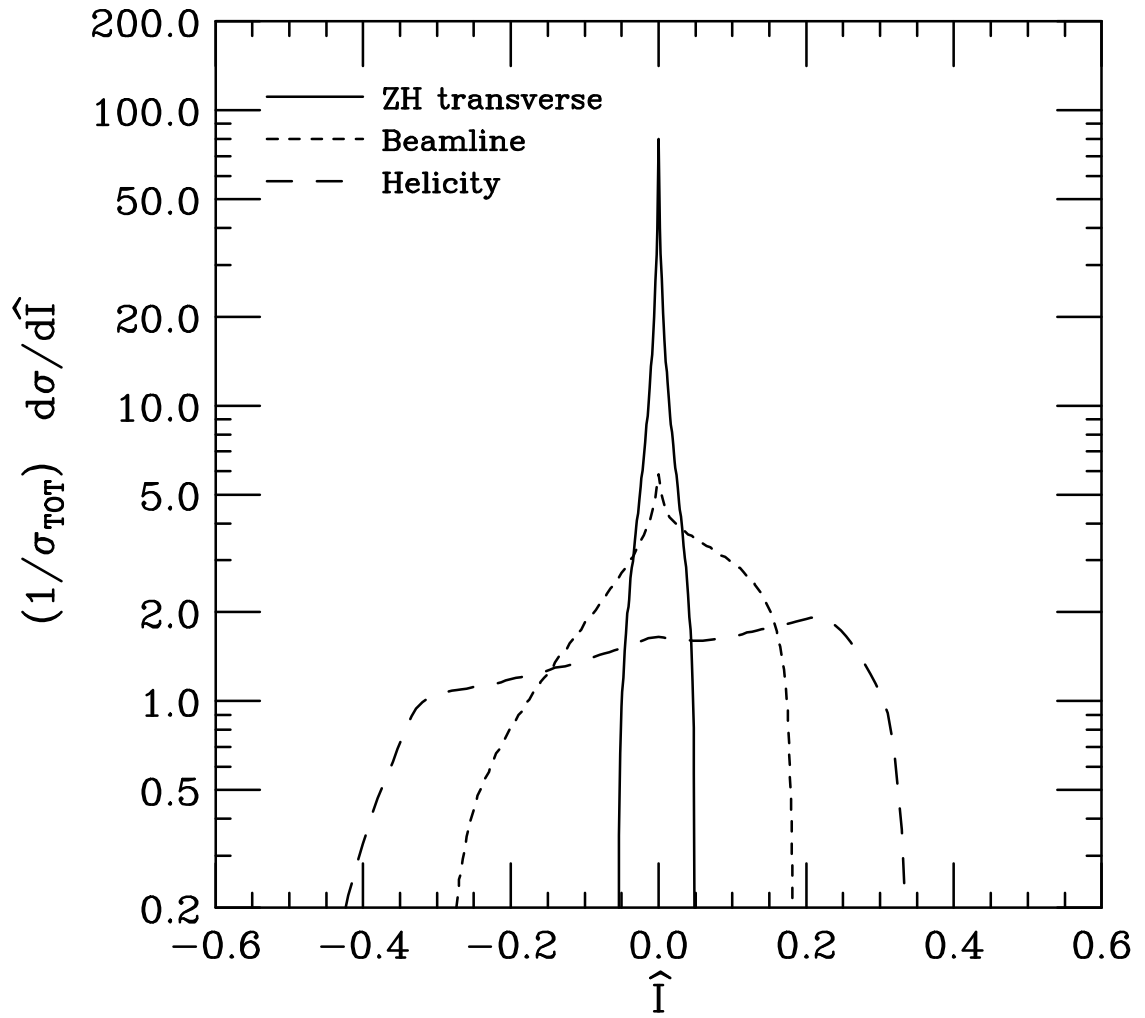


FIG. 11. The relative importance of the interference terms in the ZH -transverse, beamline and helicity bases in $e^+e^- \rightarrow ZH \rightarrow \mu^+\mu^- b\bar{b}$ at $\sqrt{s} = 192$ GeV. Plotted is the differential distribution in \hat{I} , the value of the interference term normalized to the square of the total matrix element.

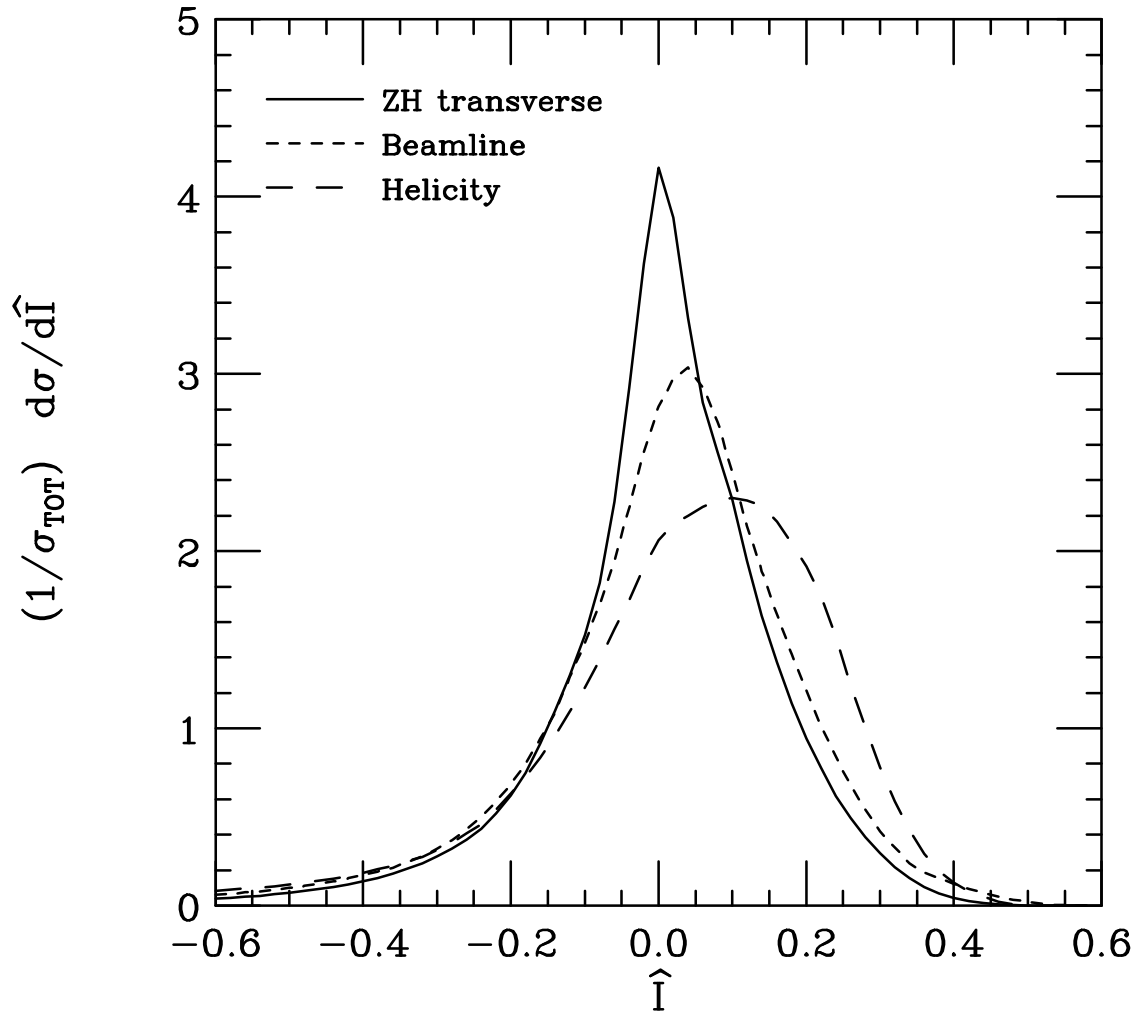


FIG. 12. The relative importance of the interference terms in the ZH -transverse, beamline and helicity bases in $e^+e^- \rightarrow ZZ \rightarrow \mu^+\mu^-b\bar{b}$ at $\sqrt{s} = 192$ GeV. Plotted is the differential distribution in \hat{I} , the value of the interference term normalized to the square of the total matrix element.

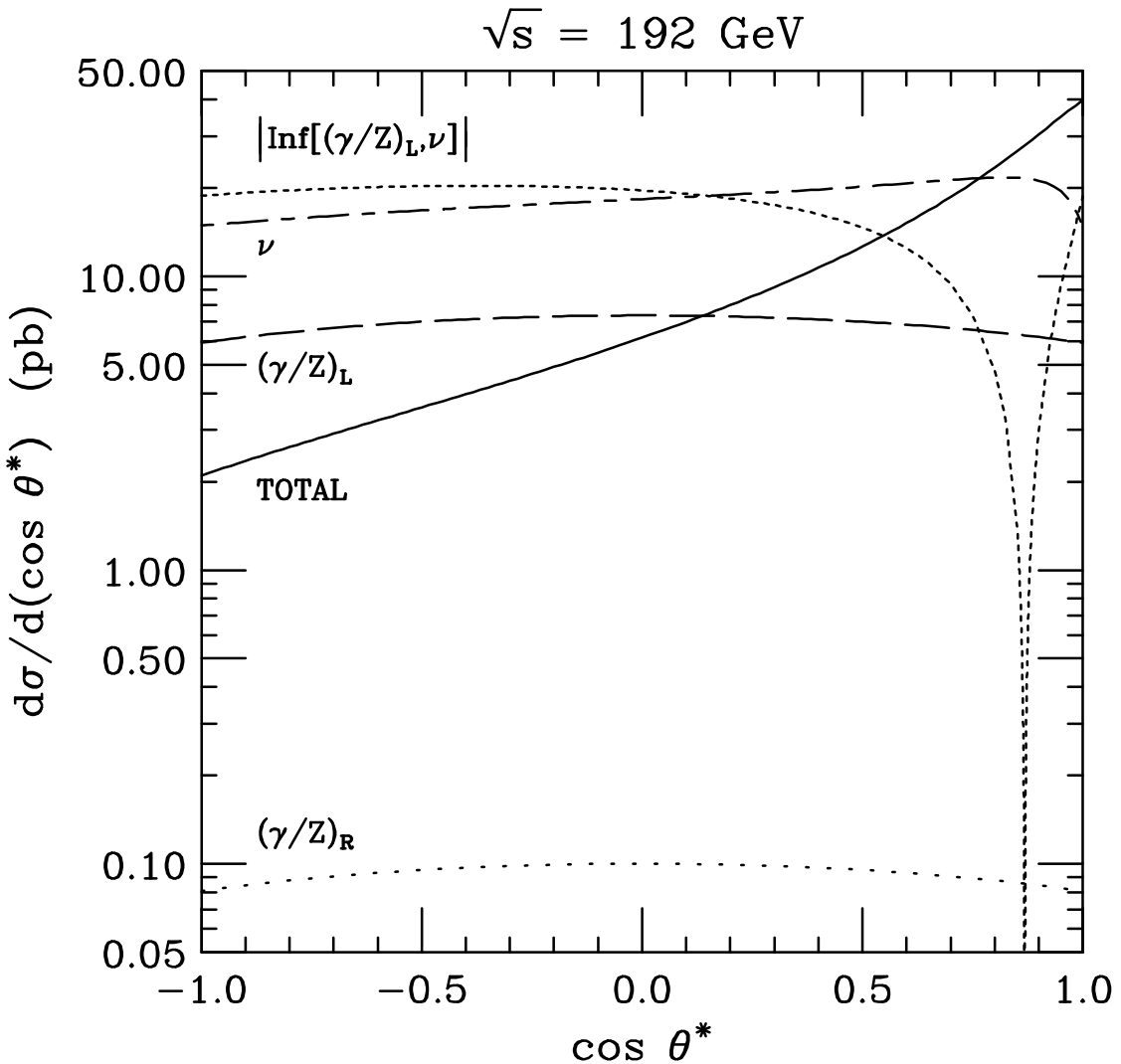


FIG. 13. Distribution in production angle of the $e^+e^- \rightarrow W^+W^-$ cross section at $\sqrt{s} = 192$ GeV. Plotted are the $(\gamma/Z)_R$, $(\gamma/Z)_L$ and neutrino contributions, plus the absolute value of the interference term between $(\gamma/Z)_L$ and ν . To the left (right) of the zero at $\cos \theta^* \approx 0.87$, the interference term is negative (positive).

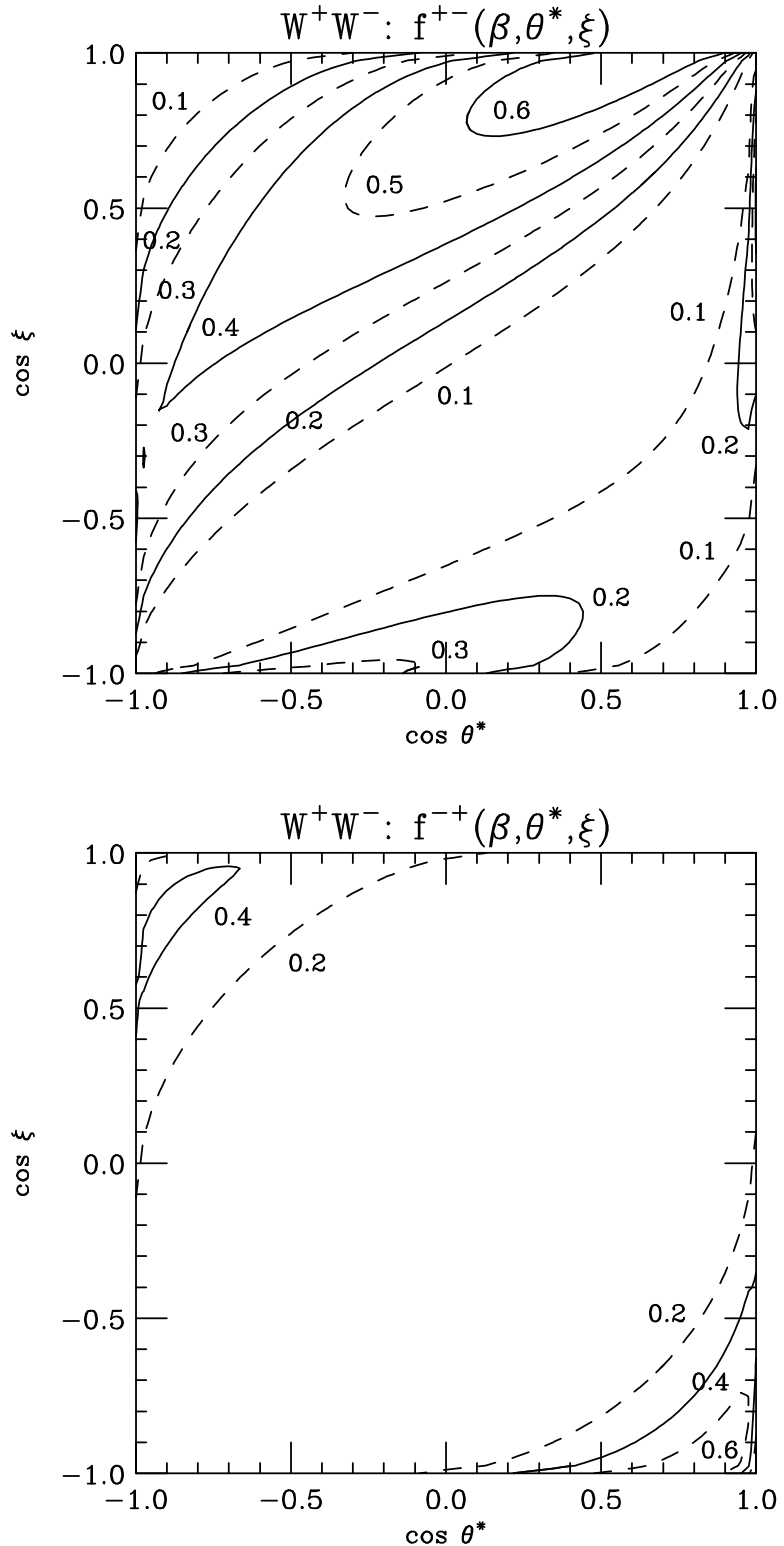


FIG. 14. Structure of the $e^+e^- \rightarrow W^+W^-$ polarized production amplitudes in the $\cos\theta^*$ - $\cos\xi$ plane for $\sqrt{s} = 192$ GeV ($\beta = 0.548$). Plotted is $f^{\lambda\bar{\lambda}}(\beta, \theta^*, \xi)$, the fraction of the total amplitude squared in each spin configuration [see Eq. (24)]. In all of the plots, $\sin\xi \geq 0$.

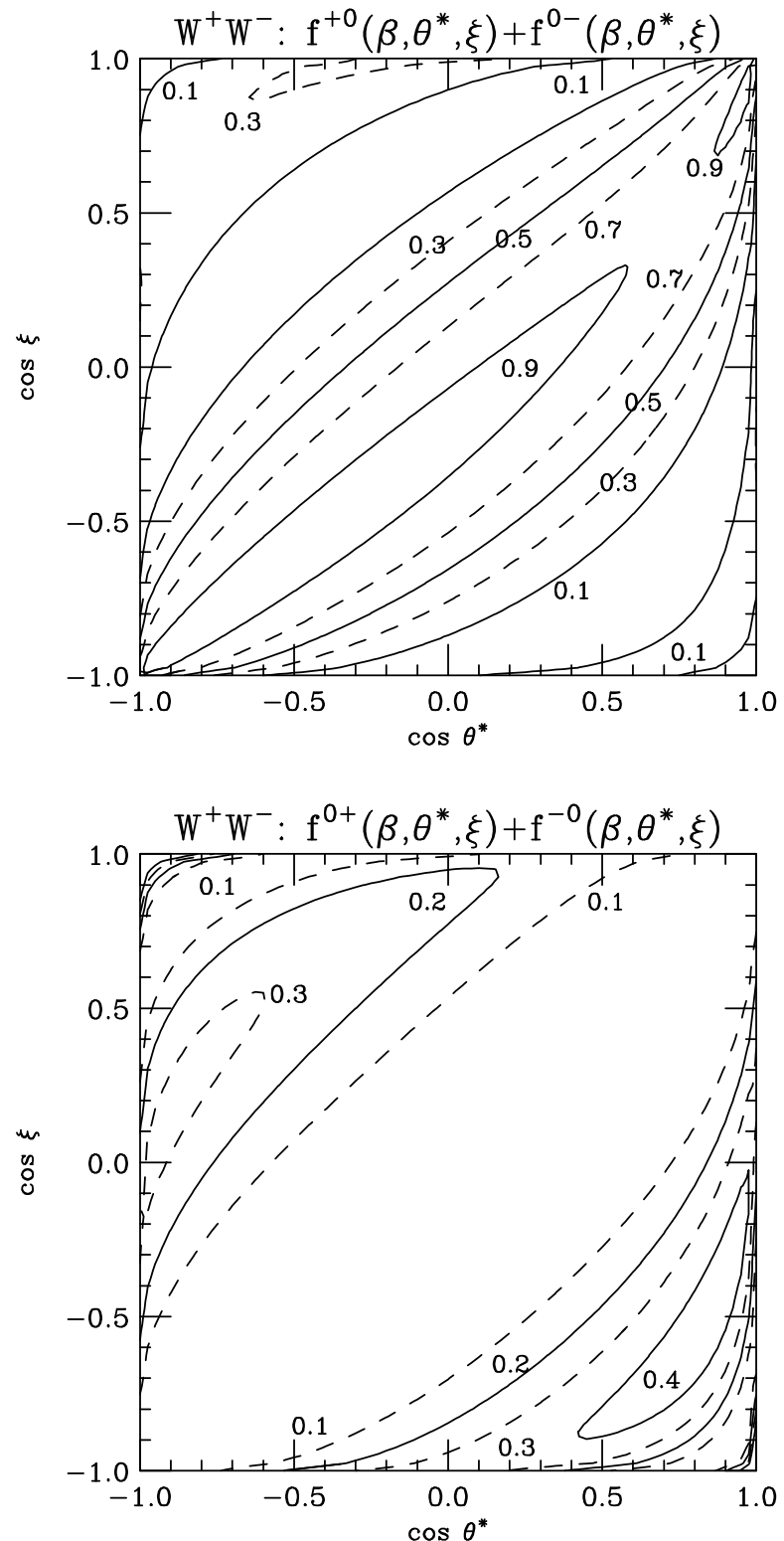


FIG. 14. (continued)

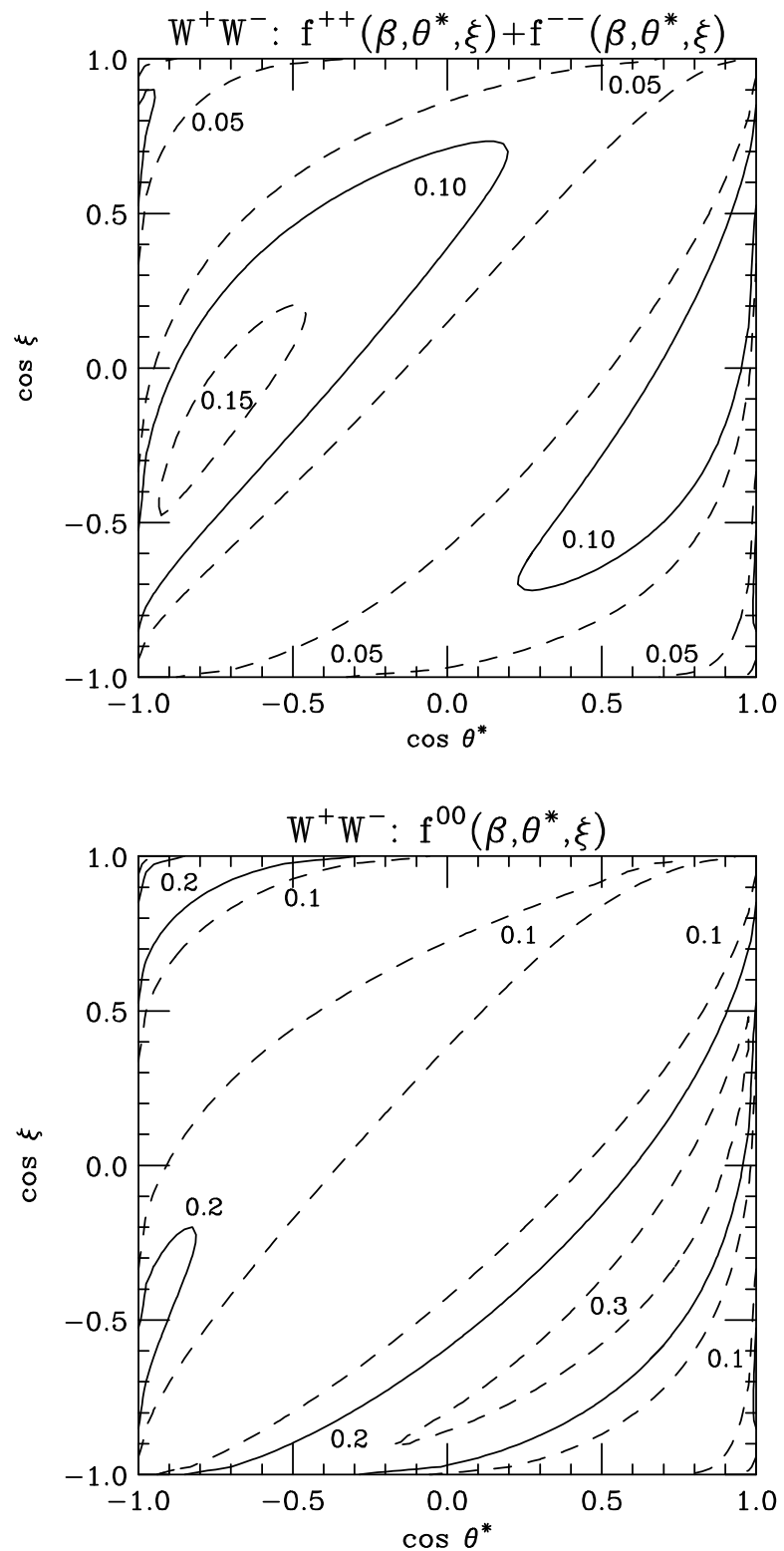


FIG. 14. (continued)

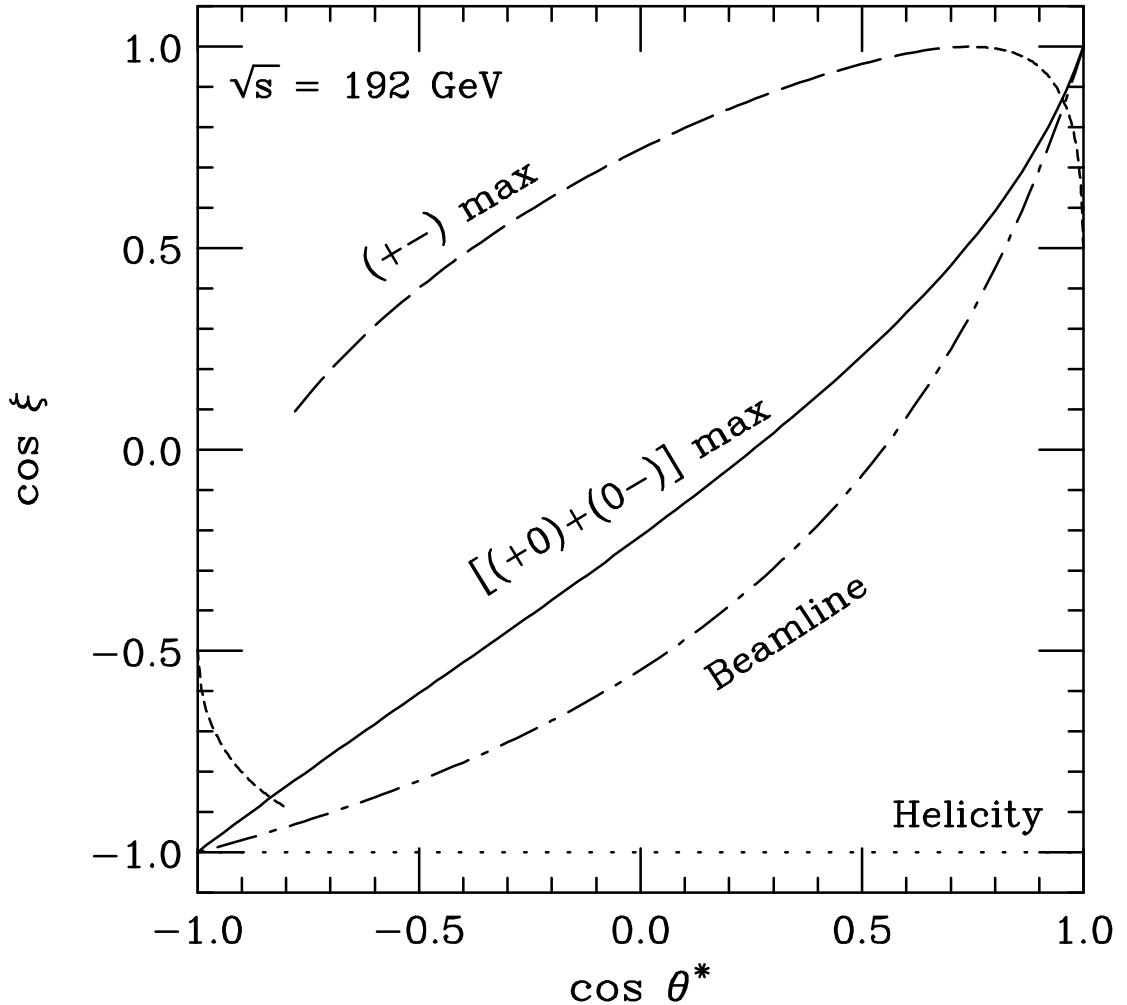


FIG. 15. The dependence of the spin angle ξ on the scattering angle θ^* for the helicity, $(+-)$ -maximized, beamline, and $[(+0) + (0-)]$ -maximized bases for W pairs produced by a 192 GeV e^+e^- collider. $\sin \xi \geq 0$ everywhere except for that portion of the $(+-)$ -maximized curve drawn with short dashes.

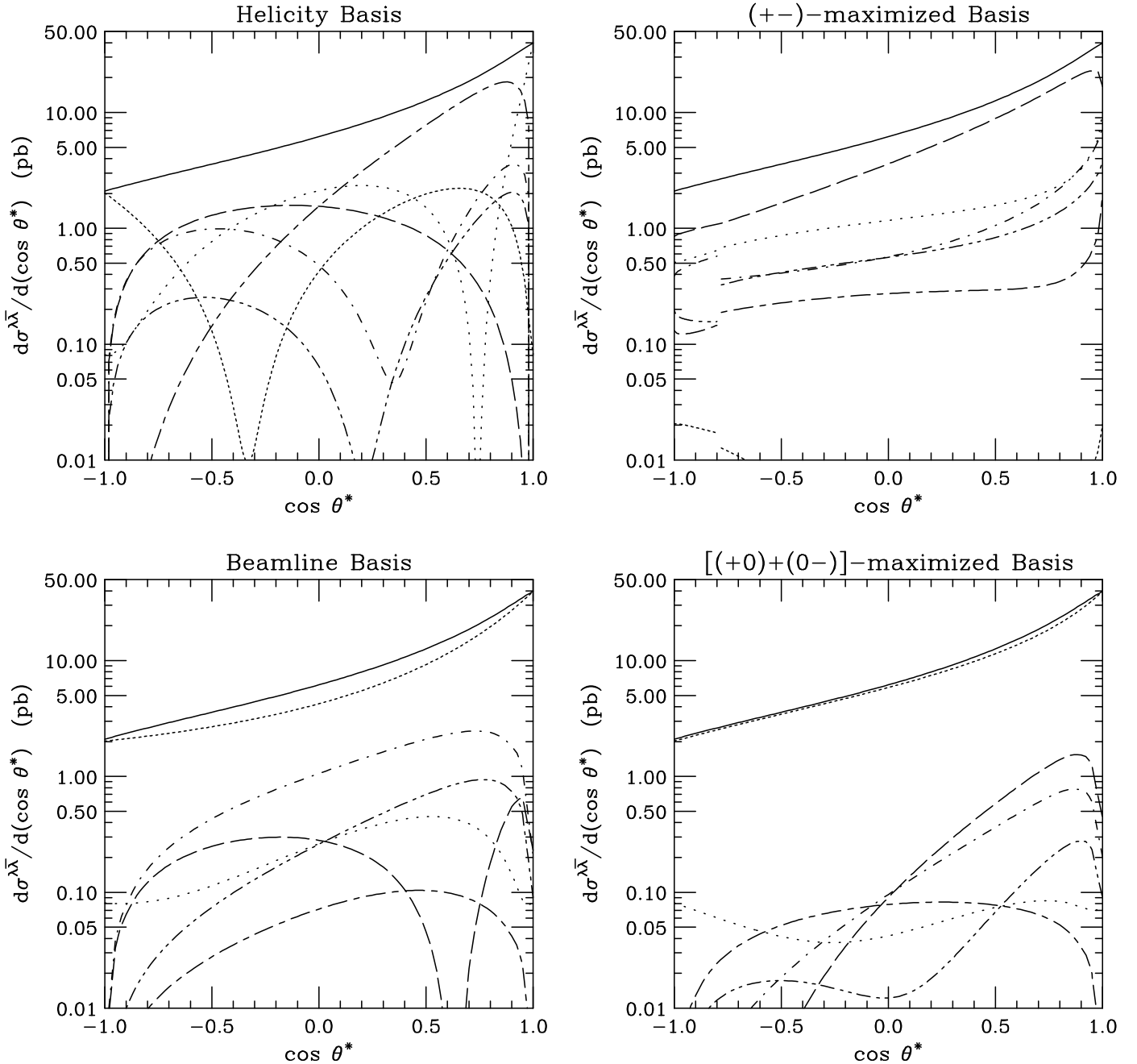


FIG. 16. Distribution in production angle of the $e^+e^- \rightarrow W\bar{W}$ cross section at $\sqrt{s} = 192$ GeV, broken down into the six independent spin combinations for the helicity, $(-+)$ -maximized, beamline, and $[(+0) + (0-)]$ -maximized bases.

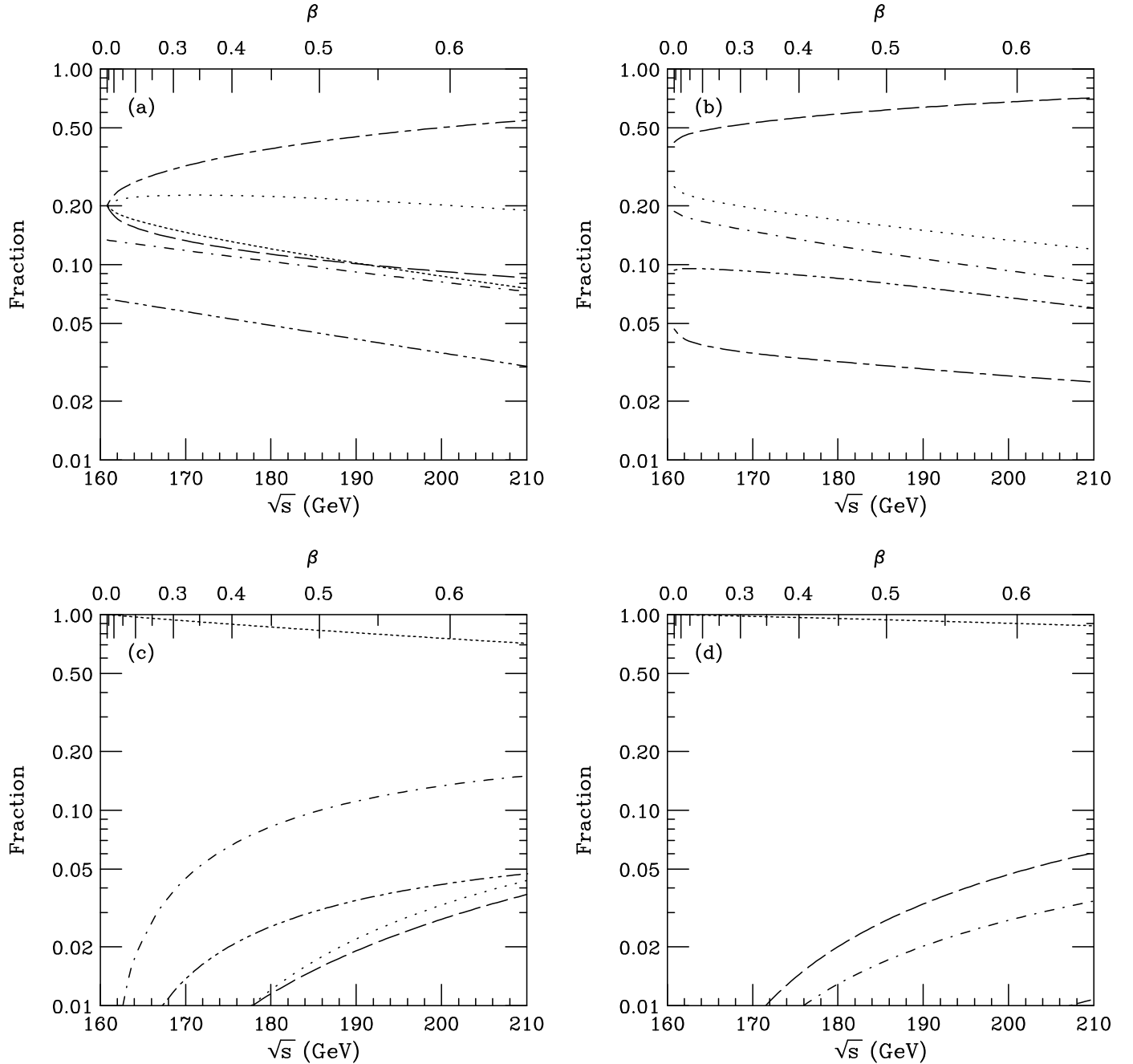


FIG. 17. Spin decomposition of the $e^+e^- \rightarrow W^+W^-$ cross section as a function of the machine energy \sqrt{s} . Shown are the fractions of the total cross section in each of the six independent spin states for the (a) helicity, (b) $(+-)$ -maximized, (c) beamline, and (d) $(+0) + (0-)$ -maximized bases. The scale along the top of these plots measures the ZMF speed β of the W bosons.

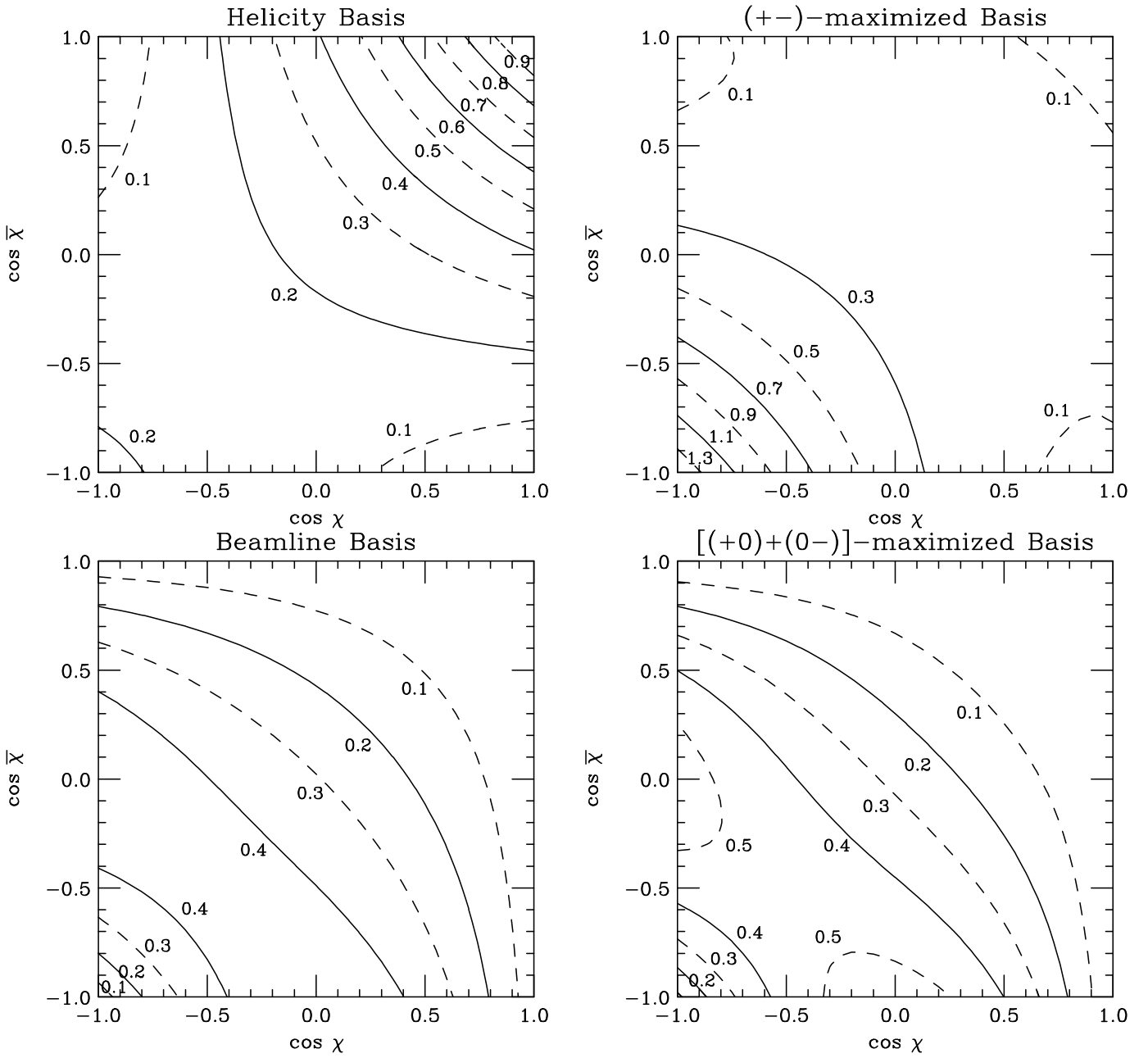


FIG. 18. Double differential decay distributions $(1/\sigma) d^2\sigma/[d(\cos \chi)d(\cos \bar{\chi})]$ for the processes $e^+e^- \rightarrow W^+W^- \rightarrow \mu^+\nu_\mu\mu^-\bar{\nu}_\mu$ in the helicity, $(-+)$ -maximized, beamline, and $[(+0) + (0-)]$ -maximized bases. χ ($\bar{\chi}$) is the angle between the μ^- (μ^+) and the spin axis, as viewed in the W^- (W^+) rest frame. For completely uncorrelated decays, this distribution would have a uniform value of $1/4$.

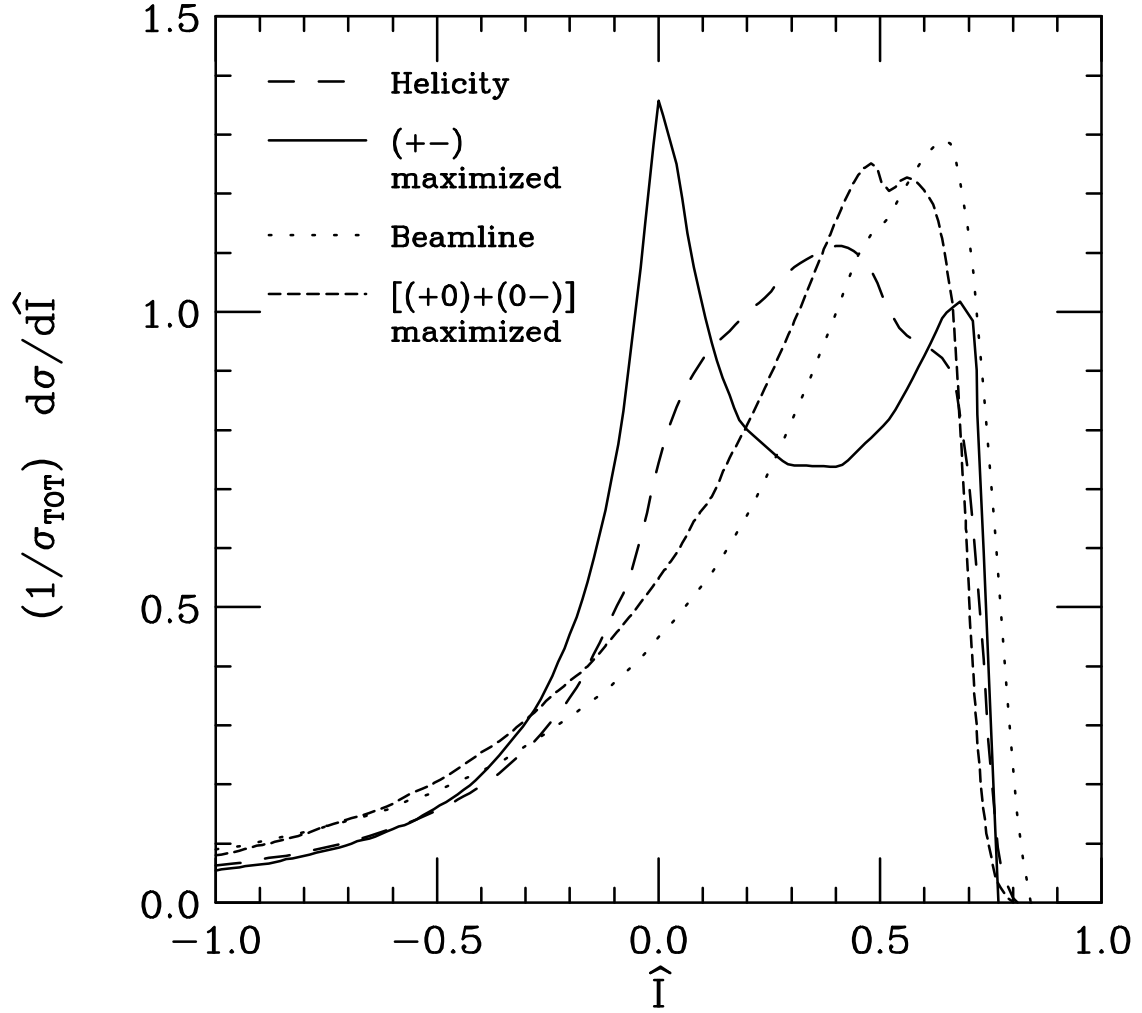


FIG. 19. The relative importance of the interference terms in the helicity, $(+-)$ -maximized, beamline, and $[(+0)+(0-)]$ -maximized bases in $e^+e^- \rightarrow W^+W^- \rightarrow \mu^+\nu_\mu\mu^-\bar{\nu}_\mu$ at $\sqrt{s} = 192$ GeV. Plotted is the differential distribution in \hat{I} , the value of the interference term normalized to the square of the total matrix element.

TABLES

TABLE I. Spin decompositions in selected bases for $e^+e^- \rightarrow ZH$ at $\sqrt{s} = 192$ GeV and $M_H = M_Z$.

Spin configuration	Helicity basis	Beamline basis	ZH -transverse basis	ZH -longitudinal basis
(0)	35.6%	3.5%	0.0% ^a	51.8%
(+)	32.2%	55.4%	57.4%	24.1%
(-)	32.2%	41.2%	42.6%	24.1%

^aThis contribution is exactly zero, by construction.

TABLE II. Spin decompositions in selected bases for $e^+e^- \rightarrow ZZ$ at $\sqrt{s} = 192$ GeV and $M_H = M_Z$. The entries in the second part of the table are the inclusive fractions obtained when we sum over all possible spins of the second Z .

Spin configuration	Helicity basis	Beamline basis	ZH -transverse basis	ZH -longitudinal basis
(00)	11.7%	5.6%	0.0% ^a	0.1%
(+-)	22.6%	4.2%	0.3%	25.7%
(-+)	22.6%	2.4%	0.2%	25.7%
(++) + (--)	5.8%	2.8%	0.0% ^a	0.0% ^a
(+0) + (0-)	18.7%	54.6%	64.1%	24.2%
(0+) + (-0)	18.7%	30.4%	35.4%	24.2%
(0+) + (00) + (0-)	30.4%	48.1%	49.7%	24.4%
(++) + (+0) + (+-)	34.8%	32.9%	32.4%	37.8%
(-+) + (-0) + (--)	34.8%	19.0%	17.9%	37.8%

^aThis component is small, but nonzero.

TABLE III. Coefficients for Z decay. The numerical values are for $\sin^2 \theta_W = 0.2315$. The final entry is for a jet of undetermined charge.

fermion	α_f	value
u, c	$\frac{(3 - 4 \sin^2 \theta_W)^2}{9 - 24 \sin^2 \theta_W + 32 \sin^4 \theta_W}$	0.834
d, s, b	$\frac{(3 - 2 \sin^2 \theta_W)^2}{9 - 12 \sin^2 \theta_W + 8 \sin^4 \theta_W}$	0.968
e, μ, τ	$\frac{(1 - 2 \sin^2 \theta_W)^2}{1 - 4 \sin^2 \theta_W + 8 \sin^4 \theta_W}$	0.574
ν	1	1.000
j	$\frac{1}{2}$	0.500

TABLE IV. Breakdown of the total cross section for the process $e^+e^- \rightarrow W^+W^-$ at tree level with $\sqrt{s} = 192$ GeV.

diagram(s)	contribution	fraction
$(\gamma/Z)_R$	0.2 pb	1.0%
$(\gamma/Z)_L$	13.8 pb	70.6%
ν	36.7 pb	188.0%
$\text{Inf}[(\gamma/Z)_L, \nu]$	-31.1 pb	-159.6%
total	19.5 pb	

TABLE V. Spin decompositions in selected bases for the total of all of the $e^+e^- \rightarrow W^+W^-$ diagrams at $\sqrt{s} = 192$ GeV.

Spin configuration	Helicity basis	(+-) maximized	Beamline basis	(+0) + (0-) maximized
(00)	8.9%	10.4%	11.6%	2.2%
(+-)	9.9%	64.6%	2.1%	3.6%
(-+)	46.2%	2.9%	0.6%	0.6%
(++) + (--)	4.0%	7.5%	3.6%	0.6%
(+0) + (0-)	9.9%	0.1%	79.7%	92.5%
(0+) + (-0)	21.1%	14.6%	2.4%	0.6%

TABLE VI. Spin decompositions in selected bases for the sum of the squares of the $(\gamma/Z)_L$ and $(\gamma/Z)_R$ contributions to $e^+e^- \rightarrow W^+W^-$ at $\sqrt{s} = 192$ GeV. As indicated in Table IV, the sum of the entries in each column is 71.6%.

Spin configuration	Helicity basis	(+-) maximized	Beamline basis	(+0) + (0-) maximized
(00)	26.8%	11.0%	1.9%	2.1%
(+-)	0.0% ^a	16.5%	30.6%	42.1%
(-+)	0.0% ^a	1.2%	0.6%	0.6%
(++) + (--)	3.6%	1.9%	3.6%	7.3%
(+0) + (0-)	20.6%	36.6%	32.5%	18.6%
(0+) + (-0)	20.6%	4.4%	2.4%	0.8%

^aThis component is exactly zero.

TABLE VII. Spin decompositions in selected bases for the square of the neutrino contribution to $e^+e^- \rightarrow W^+W^-$ at $\sqrt{s} = 192$ GeV. As indicated in Table IV, the sum of the entries in each column is 188.0%.

Spin configuration	Helicity basis	($+-$) maximized	Beamline basis	($+0$) + ($0-$) maximized
(00)	43.2%	6.3%	10.8%	0.1%
($+-$)	9.9%	110.2%	24.5%	63.9%
($-+$)	46.2%	5.6%	0.0% ^a	0.0% ^b
(++) + (--)	7.5%	7.6%	0.0% ^a	6.0%
($+0$) + ($0-$)	32.0%	36.5%	152.7%	118.0%
(0+) + (-0)	49.2%	21.8%	0.0% ^a	0.8%

^aThis component is exactly zero.

^bThis component is small, but non-zero.

TABLE VIII. Spin decompositions in selected bases for the the interference between the $(\gamma/Z)_L$ and neutrino contributions to $e^+e^- \rightarrow W^+W^-$ at $\sqrt{s} = 192$ GeV. As indicated in Table IV, the sum of the entries in each column is -159.6% .

Spin configuration	Helicity basis	($+-$) maximized	Beamline basis	($+0$) + ($0-$) maximized
(00)	-61.1%	-6.9%	-1.1%	-0.0% ^b
($+-$)	0.0% ^a	-62.2%	-53.1%	-102.5%
($-+$)	0.0% ^a	-3.9%	0.0% ^a	0.0% ^b
(++) + (--)	-7.1%	-2.0%	0.0% ^a	-12.7%
($+0$) + ($0-$)	-42.8%	-73.0%	-105.4%	-44.1%
(0+) + (-0)	-48.7%	-11.6%	0.0% ^a	-0.3%

^aThis component is exactly zero.

^bThis component is small, but non-zero, and has the indicated sign.